Computers and Fluids 203 (2020) 104493

Contents lists available at ScienceDirect

Computers and Fluids

journal homepage: www.elsevier.com/locate/compfluid

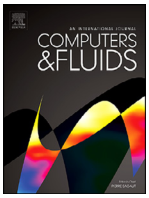

Well-balanced discontinuous Galerkin methods for the one-dimensional blood flow through arteries model with man-at-eternal-rest and living-man equilibria ☆

Jolene Britton [a], Yulong Xing [b,*]

[a] Department of Mathematics, University of California Riverside, Riverside, CA 92521, USA
[b] Department of Mathematics, Ohio State University, Columbus, OH 43210, USA

ARTICLE INFO

Article history:
Received 19 October 2019
Revised 29 January 2020
Accepted 4 March 2020
Available online 12 March 2020

Keywords:
Well-balanced methods
Discontinuous Galerkin methods
Blood flow through arteries
Steady state solutions
Shapiro number
Nearly equilibrium flow

ABSTRACT

The movement of blood flow in arteries can be modeled by a system of conservation laws and has a range of applications in medical contexts. In this paper, we present efficient well-balanced discontinuous Galerkin methods for the one-dimensional blood flow model, which preserve the man-at-eternal-rest (zero velocity) and more general living-man (non-zero velocity) equilibria. Recovery of well-balanced states, decomposition of the numerical solutions into the equilibrium and fluctuation parts, and appropriate source term and numerical flux approximations are the key ideas in designing well-balanced methods. Numerical examples are presented to verify the well-balanced property, high order accuracy, good resolution for both smooth and discontinuous solutions, and the ability to capture nearly equilibrium solutions well. We also test the proposed methods on nearly equilibrium flows with various Shapiro numbers. Man-at-eternal-rest well-balanced methods work well for problems with low Shapiro number, but generate spurious flows when Shapiro number gets larger, while the living-man well-balanced methods perform well for all ranges of Shapiro number.

1. Introduction

Blood flow models have been extensively used to mathematically understand and numerically simulate the human cardiovascular system. In 1775, Euler [9] derived a one-dimensional model of the human arterial system from the conservation of mass and momentum of the flow. Without the understanding of the wave-like nature of the flow, he noticed that the problem was too difficult to solve. Young [40] was the first to identify blood flow with wave-like behavior by finding analogous behavior between arterial blood flow wave speed and Newton's sound speed in air theories. Blood movement in arteries have flow with periodic variations known as pulsatile flow, which has been understood and explained by Lighthill [18] and Pedley [24]. Nowadays, three-dimensional mathematical models for the blood flow in arteries already exist, but the simpler one-dimensional models with averaged quantities are still of great importance [12,29,30]. The low computational cost of one-dimensional models as compared to higher dimensional models allows for one to study the wave effects within isolated segments of an artery or within the systemic arterial system (i.e. in the aorta and systemic arteries) [23,25,26,28]. Another usage of one-dimensional models is the ability to study the effects of arterial modifications, such as placements of stents and prostheses, on pulse waves [5,12]. Lastly, one-dimensional models can also be easily coupled with lumped parameter models [27] and three-dimensional fluid-structure models [10,11]. A systematic comparison of computational hemodynamics in arteries between one-dimensional and three-dimensional models with deformable vessel walls was carried out in [32], where they observed good agreement between the two models, especially during the diastolic phase of the cycle.

The one-dimensional partial differential equation (PDE) model for the blood flow through arteries [12,20,28] takes the form,

$$\begin{cases} A_t + Q_x = 0, \\ Q_t + \left(\alpha \dfrac{Q^2}{A}\right)_x + \dfrac{A}{\rho} p_x = 0, \end{cases} \tag{1.1}$$

where $A(x,t) = \pi R^2(x,t)$ is the cross-sectional area with $R(x, t) > 0$ being the radius. The variable $Q(x,t) = A(x,t)u(x,t)$ is the discharge, $u(x, t)$ denotes the flow velocity, and the constant ρ is the blood density. The parameter α is the momentum-flux correction coefficient that depends on the assumed velocity profile, and

---

☆ The work of this author was partially supported by the NSF grant DMS-1753581.

* Corresponding author.
E-mail addresses: jhout001@ucr.edu (J. Britton), xing.205@osu.edu (Y. Xing).

https://doi.org/10.1016/j.compfluid.2020.104493
0045-7930/© 2020 Elsevier Ltd. All rights reserved.

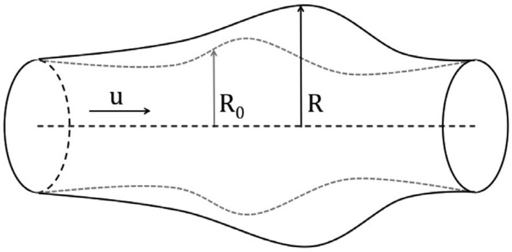

Fig. 1. Diagram of the one-dimensional blood flow model with the cross-sectional radius at rest (R_0), cross-sectional radius (R), and velocity (u).

in this paper, we take $\alpha = 1$, which means a blunt velocity profile. The source terms representing the viscous resistance of the flow and gravitational effect could be added to the system. We refer to [13] for the full description of this model.

To close the system, one needs an additional equation to link the pressure with the displacement of the vessel. A simple law describing the elastic behavior of the arterial wall is given by

$$p = p_{ext} + K(R - R_0), \quad \text{or equivalently,}$$
$$p = p_{ext} + \frac{K}{\sqrt{\pi}}\left(\sqrt{A} - \sqrt{A_0}\right), \tag{1.2}$$

where p_{ext} stands for the external pressure (assumed to be constant), the constant K represents arterial stiffness, and $A_0(x) = \pi R_0^2(x)$ is the cross-section at rest (when $u = 0$) with $R_0(x)$ being its radius. Other complex nonlinear relationship could be introduced as well. With the simple elastic law (1.2), the one-dimensional model (1.1) for the blood flow through arteries can be rewritten in the form of hyperbolic balance laws

$$\begin{cases} A_t + Q_x = 0, \\ Q_t + \left(\dfrac{Q^2}{A} + \dfrac{K}{3\rho\sqrt{\pi}}A^{\frac{3}{2}}\right)_x = \dfrac{KA}{2\rho\sqrt{\pi}\sqrt{A_0}}(A_0)_x, \end{cases} \tag{1.3}$$

which will be studied in this paper. A stent or other physical variations may cause a non-constant cross-sectional at rest $A_0(x)$, introducing a non-zero source term. A diagram of the one-dimensional blood flow model with the cross-sectional radius at rest (R_0), cross-sectional radius (R), and velocity (u) is presented in Fig. 1. For simplicity, we denote $\beta = \frac{K}{\rho\sqrt{\pi}}$ in the rest of the paper.

The PDE model (1.3) for the blood flow through arteries can be written in the convenient hyperbolic balance laws notation

$$\partial_t U + \partial_x f(U) = S(U, A_0),$$

where

$$U = \begin{pmatrix} A \\ Q \end{pmatrix}, \quad f(U) = \begin{pmatrix} Q \\ \frac{Q^2}{A} + \frac{\beta}{3}A^{\frac{3}{2}} \end{pmatrix}, \quad S(U, A_0) = \begin{pmatrix} 0 \\ \frac{\beta A}{2\sqrt{A_0}}(A_0)_x \end{pmatrix},$$

are the conservative variables, the flux, and the source term, respectively. The Jacobian matrix $\mathcal{J}(U)$ is given by

$$\mathcal{J}(U) = \begin{bmatrix} 0 & 1 \\ c^2 - \left(\dfrac{Q}{A}\right)^2 & \dfrac{2Q}{A} \end{bmatrix},$$

with $c = \sqrt{\frac{\beta\sqrt{A}}{2}}$. The eigenvalues of the Jacobian matrix are $\frac{Q}{A} \pm c$, which are real-valued and distinct [19]. This implies that the system is hyperbolic.

The system (1.3) representing the blood flow through arteries is similar to the shallow water equations (SWEs) model. This model is widely used for modeling rivers, river networks, lake flows, tides, and tsunamis. The SWEs model and the blood flow model both have two equations representing mass and momentum conservation. They belong to the family of hyperbolic balance laws, and such equations often admit non-trivial steady state solutions. These equilibria involve the perfect cancellation of the source term and the flux gradients in the PDE level, which may not be satisfied numerically due to different numerical approximations to these two terms. As a result, standard numerical methods may not be able to maintain the steady state nor capture the nearly equilibrium flow (small perturbation of the equilibrium state) well, unless a much refined mesh is used in the simulation. To resolve this issue, well-balanced methods [2] are introduced to exactly preserve the steady state solutions at the discrete level. They are often found to be efficient in capturing nearly equilibrium flow on a coarse mesh. There have been extensive studies on designing well-balanced methods for the SWEs over non-flat bottom topography [1,15,38] and Euler equations under gravitational fields [7,37].

The one-dimensional blood model through arteries (1.3) admits non-trivial steady state solutions. By definition, the steady state solutions appear when the conservative variables (A, Q) do not change over time, or equivalently, $A_t = 0$ and $Q_t = 0$ which leads to

$$\begin{cases} Q_x = 0, \\ \left(\dfrac{Q^2}{A} + \dfrac{\beta}{3}A^{\frac{3}{2}}\right)_x = \dfrac{\beta A}{2\sqrt{A_0}}(A_0)_x. \end{cases} \tag{1.4}$$

A simple steady state occurs when the velocity becomes 0, known as the *(non-zero pressure) man-at-eternal-rest* steady state or *dead-man* equilibrium in the literature

$$\left(u, \sqrt{A} - \sqrt{A_0}\right) = (0, constant). \tag{1.5}$$

A special case of this steady state appears when the pressure in (1.2) is zero. This implies that A reduces to A_0, that is,

$$(u, A) = (0, A_0). \tag{1.6}$$

We will refer to this steady state as the *zero pressure man-at-eternal-rest* steady state. The more general case occurs when the velocity u does not vanish. By some simple algebra, the general equilibrium state, denoted as the *living-man* equilibrium, can be derived as

$$\left(Q, \frac{Q^2}{2A^2} + \beta\left(\sqrt{A} - \sqrt{A_0}\right)\right) = constant. \tag{1.7}$$

One case in which this steady state might occur is in small arteries that are extremely constricted by stenosis. In this case, there is so much flow resistance that the flow loses pulsatility and approaches a steady state with non-zero velocity [14].

Various numerical methods have been designed for the one-dimensional blood flow model. A recent study [3] provides a systematic comparison of six commonly used numerical schemes for one-dimensional blood flow modelling. The numerical results are compared with theoretical results, as well as three-dimensional numerical data in compatible domains, and good agreement was observed. Recently, well-balanced methods for the blood flow through arteries which are efficient in capturing nearly equilibrium flows have gained more attention. In [8], Delestre and Lagree developed well-balanced first-order and second-order finite volume schemes for the blood flow system in elastic tubes with the man-at-eternal-rest equilibrium. They also showed the appearance of spurious flows when a simple, non-well-balanced, numerical method is used. Müller et al. [21] constructed high order well-balanced Weighted Essentially Non-Oscillatory (WENO) scheme for blood flow in elastic vessels with varying mechanical and geometrical properties. A modified version of the Dumbser–Osher–Toro Riemann solver was introduced to treat the nonconservative term, and they show the resulting methods preserves the man-at-eternal-rest equilibrium exactly. The numerical methods are then extended to networks of elastic vessels with satisfying performance. An upwind discretization for the source term to create a energy-balanced numerical solver was introduced by Murillo et al. [19]. Wang et al. [31] derived high order well-balanced finite difference WENO schemes that possess sharp shock transition. The main idea was to split the source term into two parts and approximate them with compatible WENO operators. In [16], the authors extended the hydrostatic construction idea (commonly used in the design of well-balanced methods for the SWEs) to develop high order discontinuous Galerkin (DG) and finite volume WENO scheme for the blood flow. Most of these well-balanced methods are designed to preserve the stationary man-at-eternal-rest steady state. As explained in [14], such steady states may not be that relevant for blood flow as they only occur in "dead men". For the more general living-man equilibrium state (1.7), well-balanced methods are first studied in [20], where a generalized hydrostatic reconstruction technique was used to construct the well-balanced numerical flux. In [14], Ghigo et al. presented a simple second order well-balanced method for the one-dimensional blood flow in large arteries, with two well-balanced hydrostatic reconstruction techniques designed to preserve the general steady state solutions. Numerically, the proposed methods outperform the well-balanced methods for the man-at-eternal-rest steady states based on the original hydrostatic reconstruction technique.

The work in this paper aims to develop high order well-balanced discontinuous Galerkin methods for both the man-at-eternal-rest (1.5), (1.6) and living-man (1.7) steady states of the one-dimensional blood flow model. High order accurate numerical methods are developed to provide accurate simulation on a relatively coarse mesh. DG methods, which combine the flexibility of the finite element method and stability of the finite volume method, have gained increased attention recently. Another reason we choose DG methods in this study is due to their flexibility to treat the junctions for network problems, as pointed out in [4,6], which would be important in the simulation of the human cardiovascular system. Specific advantages of the DG scheme include straightforward implementation of junction coupling conditions due to compactness and preservation of high order accuracy. Other high order methods may require stencils (wide or one-sided) that negatively impact the accuracy and stability of the scheme [6]. We start by presenting two simple approaches to design well-balanced methods for the man-at-eternal-rest steady state solution. The first approach is based on the decomposition of the numerical solution and the hydrostatic reconstruction technique, while the second one is based on the well-balanced technique in [34] to split the source term (as done in [31]). We will show the link of these two approaches, although they are derived based on different motivations. The main component of this paper is on how to design efficient well-balanced DG methods for the general living-man steady state. Special attention is paid to the projection operator to define the numerical initial condition (piecewise polynomials) of finite element methods. With a carefully chosen projection, one can recover the nonlinear living-man equilibrium states from these numerical initial conditions. Next, the numerical solutions are decomposed into two parts, one corresponding to the equilibrium component, and the other corresponding to the fluctuation. We can show that, if the living-man equilibrium is reached, this decomposition is exact in the sense that the fluctuation part becomes zero. Note that the equilibrium component is computed from the numerical solution at the current time step, and is not given a priori. With this decomposition, the modified solution values at the cell interface can be defined, which can recover the exact equilibrium solutions when the equilibrium state is reached. The general hydrostatic reconstruction idea is then adopted to provide the well-balanced numerical flux. Together with a careful choice of the source term approximation, well-balanced DG methods for the general living-man equilibrium can be designed.

The paper is organized as follows. In Section 2, the necessary notations are introduced and well-balanced DG methods to preserve the man-at-eternal-rest steady state are discussed. Section 3 presents the numerical performance of the DG methods in Section 2. The well-balanced DG methods that maintain the more general living-man equilibrium state of the blood flow model are discussed in Section 4. In Section 5, numerical examples are given to demonstrate the high-order accuracy, well-balanced property, and good resolution for smooth and discontinuous solution of the methods described in Section 4. Concluding remarks are found in Section 6.

2. Man-at-eternal-rest well-balanced DG schemes

We start by presenting well-balanced DG scheme for the simpler man-at-eternal-rest steady states (1.5), (1.6). The proposed methods will be extended to the general living-man equilibrium (1.7) in Section 4.

2.1. Notations and discontinuous Galerkin methods

The computational domain, denoted by I, will be discretized into J cells. The point x_j, for $j = 1, \dots, J$, is the center of the cell $I_j = [x_{j-\frac{1}{2}}, x_{j+\frac{1}{2}}]$. The size of the j^{th} cell is denoted by $\Delta x_j = x_{j+\frac{1}{2}} - x_{j-\frac{1}{2}}$. Furthermore, we let $h = \max_j \Delta x_j$. We seek an approximation U_h of the solution U, which belongs to the finite dimensional space

$$\mathbb{V}_h^k = \{v : v|_{I_j} \in P^k(I_j),\ j = 1, \dots, J\}, \tag{2.1}$$

where $P^k(I)$ is the space of polynomials in I of degree up to k. The cross-sectional area at rest, A_0, will also be projected into $\mathbb{V}_h^k$, and we denote it by $(A_0)_h$. The value of U_h may not be continuous at the cell interface $x_{j+\frac{1}{2}}$, thus we denote $U^+_{h,j+\frac{1}{2}} = \begin{pmatrix} A^+_{h,j+\frac{1}{2}} \\ Q^+_{h,j+\frac{1}{2}} \end{pmatrix}$ as the limit from the right cell I_{j+1} and $U^-_{h,j+\frac{1}{2}} = \begin{pmatrix} A^-_{h,j+\frac{1}{2}} \\ Q^-_{h,j+\frac{1}{2}} \end{pmatrix}$ as the limit from the left cell I_j.

The traditional DG scheme, which may not be well-balanced, can be written as

$$\int_{I_j} \partial_t U_h v \, dx - \int_{I_j} f(U_h) \partial_x v \, dx + \hat{f}_{j+\frac{1}{2}} v^-_{j+\frac{1}{2}} - \hat{f}_{j-\frac{1}{2}} v^+_{j-\frac{1}{2}} = \int_{I_j} S(U_h, (A_0)_h) v \, dx, \tag{2.2}$$

where $v(x)$ is a test function from the test space $\mathbb{V}_h^k$, and

$$\hat{f}_{j+\frac{1}{2}} = F\left(U^-_{h,j+\frac{1}{2}}, U^+_{h,j+\frac{1}{2}}\right).$$

Here the function $F(a, b)$ is the numerical flux, which takes information from both the left and right side of the cell interface. We implement the simple Lax–Friedrichs flux

$$F(a, b) = \frac{1}{2}(f(a) + f(b) - \alpha(b - a)), \tag{2.3}$$

where $\alpha = \max_{U_h}(\frac{Q_h}{A_h} + \sqrt{\frac{\beta\sqrt{A_h}}{2}})$ is derived from determining the eigenvalues of the Jacobian matrix of $f(U)$. The maximum in the calculation of α can be taken either over the entire computational domain or locally.

The scheme (2.2) is a semi-discrete method. For the temporal discretization, the high order total variation diminishing (TVD) Runge-Kutta time discretization can be used. Throughout this paper the third order TVD Runge-Kutta method,

$$U_h^{(1)} = U_h^n + \Delta t \mathcal{F}(U_h^n),$$

$$
\begin{aligned}
U_h^{(2)} &= \frac{3}{4}U_h^n + \frac{1}{4}\left(U_h^{(1)} + \Delta t\mathcal{F}\left(U_h^{(1)}\right)\right),\\
U_h^{n+1} &= \frac{1}{3}U_h^n + \frac{2}{3}\left(U_h^{(2)} + \Delta t\mathcal{F}\left(U_h^{(2)}\right)\right).
\end{aligned}
\tag{2.4}
$$

with spatial operator $\mathcal{F}$ defined as the terms in (2.2) except the one containing the time derivative, is used. This completes the description of a fully discrete high order Runge-Kutta discontinuous Galerkin (RKDG) method.

Our goal is to design well-balanced DG methods which can preserve the man-at-eternal-rest steady states (1.5) and (1.6). Many different approaches to design well-balanced methods have been studied in the literature, mostly for the shallow water equations with non-flat bottom topography. The key idea of well-balanced methods in this paper is to decompose the numerical solution at each time step into the equilibrium part and the fluctuation part, which has also been studied in [33]. We carefully choose the decomposition so that, if the steady state is reached, the equilibrium part recovers the steady state perfectly. Then by approximating the contribution of the equilibrium part and the fluctuation part in the source term in a different way, one can achieve well-balanced property. The details are given below. We would like to comment that this approach is somehow similar to that of solving the new PDE with the unknown being the perturbation to the equilibrium state. The main difference is that our approach does not assume the explicit knowledge of the equilibrium state a priori, and we recover that equilibrium part (more specifically, the constant values in (1.7)) numerically.

In the framework of DG methods, all of the numerical solutions (including U_h and $(A_0)_h$) are discontinuous at the cell interfaces, even at the steady state. To address this, we follow the idea of hydrostatic reconstruction, and present our well-balanced numerical scheme in the form of

$$
\begin{aligned}
&\int_{I_j}\partial_t U_h^n v\,dx - \int_{I_j} f(U_h^n)\partial_x v\,dx + \hat{f}_{j+\frac{1}{2}}v^-_{j+\frac{1}{2}} - \hat{f}_{j-\frac{1}{2}}v^+_{j-\frac{1}{2}}\\
&\quad= \int_{I_j} S(U_h^n,(A_0)_h)v\,dx + (\hat{f}_{j+\frac{1}{2}} - \hat{f}^l_{j+\frac{1}{2}})v^-_{j+\frac{1}{2}} - (\hat{f}_{j-\frac{1}{2}} - \hat{f}^r_{j-\frac{1}{2}})v^+_{j-\frac{1}{2}},
\end{aligned}
\tag{2.5}
$$

where $\hat{f}_{j+\frac{1}{2}} - \hat{f}^l_{j+\frac{1}{2}}$ and $\hat{f}_{j-\frac{1}{2}} - \hat{f}^r_{j-\frac{1}{2}}$ are high order correction terms at the level of $O(\Delta x^{k+1})$ when A_0 is smooth, regardless of the smoothness of the solution U_h. The design of $\hat{f}^l_{j+\frac{1}{2}}$ and $\hat{f}^r_{j-\frac{1}{2}}$, known as the left and right fluxes, are central to this scheme and will be discussed in the following subsection. The scheme (2.5) is a spatially $(k+1)$-th order conservative scheme and is equivalent to the more compact formulation

$$
\begin{aligned}
&\int_{I_j}\partial_t U_h^n v\,dx - \int_{I_j} f(U_h^n)\partial_x v\,dx + \hat{f}^l_{j+\frac{1}{2}}v^-_{j+\frac{1}{2}}\\
&\qquad - \hat{f}^r_{j-\frac{1}{2}}v^+_{j-\frac{1}{2}} = \int_{I_j} S(U_h^n,(A_0)_h)v\,dx.
\end{aligned}
\tag{2.6}
$$

A similar form has been described to obtain well-balanced methods for the shallow water equations [39] and for the blood flow model [16].

The focus of the following subsections will be on defining the left and right fluxes as well as presenting how the source term is evaluated. To illustrate the approaches, we will start with the simpler zero pressure man-at-eternal-rest case (1.6) in Section 2.2. The non-zero pressure man-at-eternal-rest case (1.5) will be discussed in Section 2.3.

2.2. The zero pressure man-at-eternal-rest well-balanced scheme

2.2.1. Well-balanced numerical fluxes

First, at each time step, we decompose the conservative unknown variables U_h into the sum of a reference equilibrium state U_h^e and a fluctuation part U_h^f. Taking the zero pressure man-at-eternal-rest steady state (1.6) in consideration, we can define the equilibrium part of the conservative variables in I_j by

$$
U_{h,j}^e(x) = \begin{pmatrix} A_{h,j}^e(x)\\ Q_{h,j}^e(x)\end{pmatrix} = \begin{pmatrix} (A_0)_{h,j}(x)\\ 0\end{pmatrix},
\tag{2.7}
$$

since the equilibrium state is explicitly given. The fluctuation part U_h^f can be determined by the decomposition of the summation

$$
U_h = U_h^e + U_h^f,
\tag{2.8}
$$

which leads to

$$
U_{h,j}^f(x) = \begin{pmatrix} A_{h,j}^f(x)\\ Q_{h,j}^f(x)\end{pmatrix} = \begin{pmatrix} A_{h,j}(x) - (A_0)_{h,j}(x)\\ Q_{h,j}(x)\end{pmatrix}.
\tag{2.9}
$$

When the solution is at a steady state, one can observe that the equilibrium parts U_h^e are equivalent to U_h, hence $U_h^f = 0$. The notations of U_h^e and U_h^f are introduced here to be consistent with those in the living-man well-balanced methods in Section 4, and are not necessary for this simpler man-at-eternal-rest steady state problem.

The idea of hydrostatic reconstruction is used for computing the numerical fluxes. It was first introduced by Audusse in [1]. At time step t^n, the cell interface values $U^\pm_{h,j+\frac{1}{2}}$ are computed first. We construct the cell interface value of A_0 as

$$
(A_0)^*_{h,j+\frac{1}{2}} = \max\left((A_0)^+_{h,j+\frac{1}{2}}, (A_0)^-_{h,j+\frac{1}{2}}\right),
\tag{2.10}
$$

and use it to evaluate the modified cell interface values of A_h

$$
\begin{aligned}
A^{*,-}_{h,j+\frac{1}{2}} &= \max\left((A_0)^*_{h,j+\frac{1}{2}} + A^{f,-}_{h,j+\frac{1}{2}}, 0\right)\\
&= \max\left(A^-_{h,j+\frac{1}{2}} - (A_0)^-_{h,j+\frac{1}{2}} + (A_0)^*_{h,j+\frac{1}{2}}, 0\right),\\
A^{*,+}_{h,j+\frac{1}{2}} &= \max\left((A_0)^*_{h,j+\frac{1}{2}} + A^{f,+}_{h,j+\frac{1}{2}}, 0\right)\\
&= \max\left(A^+_{h,j+\frac{1}{2}} - (A_0)^+_{h,j+\frac{1}{2}} + (A_0)^*_{h,j+\frac{1}{2}}, 0\right).
\end{aligned}
\tag{2.11}
$$

The new cell boundary values for U are then defined as

$$
U^{*,\pm}_{h,j+\frac{1}{2}} = \begin{pmatrix} A^{*,\pm}_{h,j+\frac{1}{2}}\\ Q^\pm_{h,j+\frac{1}{2}}\end{pmatrix}.
\tag{2.12}
$$

Lastly, the left and right fluxes are determined in the following manner

$$
\begin{aligned}
\hat{f}^l_{j+\frac{1}{2}} &= F\left(U^{*,-}_{h,j+\frac{1}{2}}, U^{*,+}_{h,j+\frac{1}{2}}\right) + \begin{pmatrix} 0\\ \frac{\beta}{3}(A^-_{h,j+\frac{1}{2}})^{\frac{3}{2}} - \frac{\beta}{3}(A^{*,-}_{h,j+\frac{1}{2}})^{\frac{3}{2}}\end{pmatrix},\\
\hat{f}^r_{j-\frac{1}{2}} &= F\left(U^{*,-}_{h,j-\frac{1}{2}}, U^{*,+}_{h,j-\frac{1}{2}}\right) + \begin{pmatrix} 0\\ \frac{\beta}{3}(A^+_{h,j-\frac{1}{2}})^{\frac{3}{2}} - \frac{\beta}{3}(A^{*,+}_{h,j-\frac{1}{2}})^{\frac{3}{2}}\end{pmatrix}.
\end{aligned}
\tag{2.13}
$$

The choice of $U^{*,\pm}_{h,j+\frac{1}{2}}$ was defined in the way such that they are the same at the cell interfaces when steady state is reached, which is desirable for achieving the well-balanced property. Notice that at the steady state, the left and right fluxes simplify to $\hat{f}^l_{j+\frac{1}{2}} = f(U^-_{h,j+\frac{1}{2}})$ and $\hat{f}^r_{j-\frac{1}{2}} = f(U^+_{h,j-\frac{1}{2}})$ as a result of the numerical flux F being consistent.

2.2.2. Source term approximation

In an effort to balance the source term with the numerical fluxes, an approximation of the source term will be discussed in this section. The source term $S(U, A_0) = \frac{\beta A}{2\sqrt{A_0}}(A_0)_x = \beta A(\sqrt{A_0})_x$ is linear with respect to the variable A. As a result of this linearity and the decomposition of U_h in (2.8), the source term can be decomposed as

$$\int S(U_h,(A_0)_h)v\,dx = \int S\big(U_h^e,(A_0)_h\big)v\,dx + \int S\big(U_h^f,(A_0)_h\big)v\,dx. \tag{2.14}$$

The second term on the right hand side can be directly computed by a quadrature rule. On the other hand, since the function $U_h^e(x)$ is the equilibrium state, we recall the following relation

$$\int_{I_j} S\big(U_h^e,(A_0)_h\big)v\,dx = -\int_{I_j} f\big(U_h^e\big)v_x\,dx + f\left(U^{e,-}_{h,j+\frac{1}{2}}\right)v^-_{j+\frac{1}{2}} - f\left(U^{e,+}_{h,j-\frac{1}{2}}\right)v^+_{j-\frac{1}{2}}, \tag{2.15}$$

holds. When a quadrature rule is used for numerical integration, this equality holds approximately, up to the accuracy of the quadrature rule. For the purpose of well-balancedness, we cannot use (2.14) with a quadrature rule to approximate the source term, instead, the approximation for the source term will be evaluated by

$$\int_{I_j} S(U_h,(A_0)_h)v\,dx = -\int_{I_j} f\big(U_h^e\big)v_x\,dx + f\left(U^{e,-}_{h,j+\frac{1}{2}}\right)v^-_{j+\frac{1}{2}} - f\left(U^{e,+}_{h,j-\frac{1}{2}}\right)v^+_{j-\frac{1}{2}} + \int_{I_j} S\big(U_h^f,(A_0)_h\big)v\,dx. \tag{2.16}$$

Taking the choice of U_h^e in (2.7), the decomposition of the source term (2.14) becomes

$$\int \beta A_h(\sqrt{(A_0)_h})_x v\,dx = \int \beta A_0(\sqrt{(A_0)_h})_x v\,dx + \int \beta(A_h-(A_0)_h)(\sqrt{(A_0)_h})_x v\,dx, \tag{2.17}$$

and the approximation for the source term in (2.16) reduces to

$$\int_{I_j} \beta A_h(\sqrt{A_0})_x v\,dx = -\int_{I_j}\frac{\beta}{3}((A_0)_h)^{\frac{3}{2}}v_x\,dx + \frac{\beta}{3}\left((A_0)^-_{h,j+\frac{1}{2}}\right)^{\frac{3}{2}}v^-_{j+\frac{1}{2}} - \frac{\beta}{3}\left((A_0)^+_{h,j-\frac{1}{2}}\right)^{\frac{3}{2}}v^+_{j-\frac{1}{2}} + \int_{I_j}(A_h-(A_0)_h)(\sqrt{(A_0)_h})_x v\,dx. \tag{2.18}$$

Remark 2.1. The source term used in this paper is due to only the cross-sectional area at rest. The decomposition (2.14) will not hold if the source term also included a friction term or another term that is not linear with respect to the conservative variables. However, one could consider a similar decomposition for the source term as follows

$$\int S(U_h,(A_0)_h)v\,dx = \int S\big(U_h^e,(A_0)_h\big)v\,dx + \int \Big(S(U_h,(A_0)_h) - S\big(U_h^e,(A_0)_h\big)\Big)v\,dx. \tag{2.19}$$

The first term on the right hand side, $\int S\big(U_h^e,(A_0)_h\big)v\,dx$, can be approximated by (2.15). The second term on the right hand side can be computed using numerical integration with an appropriate quadrature scheme. It is interesting to note that $S(U_h,(A_0)_h) - S\big(U_h^e,(A_0)_h\big) = S\big(U_h - U_h^e,(A_0)_h\big) = S\Big(U_h^f,(A_0)_h\Big)$ when the source term is linear, and this leads to the original source decomposition formulation.

Remark 2.2. In the well-balanced methods designed for the SWEs in [35], a straightforward numerical integration of the source term by a quadrature rule accurate for polynomial of degree $3k-1$ is sufficient. This is due to the fact that the Eq. (2.15) holds exactly with sufficiently accurate quadrature, therefore, Eqs. (2.14) and (2.16) are equivalent. For the blood flow with a source term of the form $S(U_h,(A_0)_h) = \frac{\beta A_h}{2\sqrt{(A_0)_h}}((A_0)_h)_x$, a direct numerical integral with quadrature rules does not yield a well-balanced method, because $\sqrt{(A_0)_h}$ is no longer a polynomial, hence any numerical integration may not be exact. For the steady state problem, the numerical error would be dominated by the integration error, which becomes non-negligible, especially on a coarse mesh.

We conclude this subsection by showing the scheme indeed satisfies the well-balanced property.

Proposition 1. *The DG scheme (2.6) for the blood flow system (1.3) with the zero pressure man-at-eternal-rest steady state (1.6) is well-balanced when paired with the numerical fluxes (2.13) and the source term decomposition (2.16).*

Proof. At the steady state, we have $U_h^f = 0$ and $U_h^e = U_h$. The approximation (2.16) to the source term becomes

$$\begin{aligned}\int_{I_j} S(U_h,(A_0)_h)v\,dx &= -\int_{I_j} f\big(U_h^e\big)v_x\,dx + f\left(U^{e,-}_{h,j+\frac{1}{2}}\right)v^-_{j+\frac{1}{2}} - f\left(U^{e,+}_{h,j-\frac{1}{2}}\right)v^+_{j-\frac{1}{2}}\\ &= -\int_{I_j} f(U_h)v_x\,dx + f\left(U^{-}_{h,j+\frac{1}{2}}\right)v^-_{j+\frac{1}{2}} - f\left(U^{+}_{h,j-\frac{1}{2}}\right)v^+_{j-\frac{1}{2}}.\end{aligned} \tag{2.20}$$

Additionally, the left and right fluxes (2.13) simplify to $\hat{f}^l_{j+\frac{1}{2}} = f\left(U^-_{h,j+\frac{1}{2}}\right)$ and $\hat{f}^r_{j-\frac{1}{2}} = f\left(U^+_{h,j-\frac{1}{2}}\right)$ at the steady state. Therefore, we have shown the fluxes and source term balance, which implies the scheme is indeed well-balanced. □

2.2.3. An alternative zero pressure man-at-eternal-rest well-balanced DG scheme

In this subsection, we present an alternative well-balanced DG method for the zero pressure man-at-eternal-rest steady state (1.6). This follows the idea of decomposing the source term, proposed first in [34] for the shallow water equation, and later in [17,36] for a general class of hyperbolic balance laws. The same idea has been studied in [31] to develop well-balanced finite difference WENO scheme for the blood flow model.

The key idea is to introduce the following source term decomposition,

$$\frac{\beta A}{2\sqrt{A_0}}(A_0)_x = \beta(A-A_0)\left(\sqrt{A_0}\right)_x + \left(\frac{\beta}{3}A_0^{\frac{3}{2}}\right)_x, \tag{2.21}$$

and we refer to [36] for the motivation of such decomposition. Note that this coincides with the source term approximation (2.18), although they arise from different approaches. We can then move the term $\left(\frac{\beta}{3}A_0^{\frac{3}{2}}\right)_x$ to the left side and combine it with the flux to achieve the updated equation of the form

$$\begin{cases} A_t + Q_x = 0,\\ Q_t + \left(\dfrac{Q^2}{A} + \dfrac{\beta}{3}A^{\frac{3}{2}} - \dfrac{\beta}{3}A_0^{\frac{3}{2}}\right)_x = \beta(A-A_0)\left(\sqrt{A_0}\right)_x, \end{cases} \tag{2.22}$$

It is clear that at the zero pressure man-at-eternal-rest steady state $(Q,A) = (0,A_0)$, the system of PDEs (2.22) has both zero flux and source term, hence the traditional DG scheme (2.2) is automatically well-balanced when the Lax–Friedrichs fluxes defined in (2.3) is updated to be

$$F(U_h^-, U_h^+) = \frac{1}{2}\left(f(U_h^-) + f(U_h^+) - \alpha\left(\begin{pmatrix} A_h^+ - (A_0)_h^+ \\ Q_h^+ \end{pmatrix} - \begin{pmatrix} A_h^- - (A_0)_h^- \\ Q_h^- \end{pmatrix} \right)\right), \tag{2.23}$$

so that the added numerical diffusion term disappears at the steady state. Note that f in (2.23) now corresponds to the flux in the updated form (2.22). The proof of the well-balanced property is rather straightforward and is not included here.

This is a simple approach to achieve well-balanced property, and there is no need to introduce the hydrostatic reconstruction idea when constructing the numerical fluxes. However, this cannot be extended to the more complicated living-man equilibrium case.

2.3. The non-zero pressure man-at-eternal-rest well-balanced scheme

In this section, we present well-balanced DG methods for the man-at-eternal-rest steady state with non-zero pressure (1.5).

We start with the description of well-balanced numerical fluxes. For the non-zero pressure man-at-eternal-rest steady state (1.5), the choice of the decomposition into U_h^e and U_h^f, as well as the definition of $A^{*,\pm}_{h,j+\frac{1}{2}}$ must be modified from those presented in the previous subsection. The decomposed variables will be computed based on the steady state solution (1.5), therefore we denote $V = \binom{Q}{E} = \binom{Q}{\sqrt{A}-\sqrt{A_0}}$ to be the equilibrium variables. The reference equilibrium values $\hat{V}$ in each cell I_j are defined by the following,

$$\hat{V}_j = \begin{pmatrix} \hat{Q}_j \\ \hat{E}_j \end{pmatrix} = \begin{pmatrix} Q_h\left(x^-_{j+\frac{1}{2}}\right) \\ \left(\sqrt{A_{h,j}} - \sqrt{(A_0)_{h,j}}\right)\left(x^-_{j+\frac{1}{2}}\right) \end{pmatrix}, \tag{2.24}$$

which will be constant for all j if the system is at a steady state. It follows that the equilibrium part $U^e_{h,j}$ can be defined using $\hat{V}_j$ and the true value of $A_0(x)$,

$$U^e_{h,j}(x) = \begin{pmatrix} A^e_{h,j}(x) \\ Q^e_{h,j}(x) \end{pmatrix} = \begin{pmatrix} \mathbb{P}\left(\left(\hat{E}_j + \sqrt{A_0(x)}\right)^2\right) \\ \hat{Q}_j \end{pmatrix}, \tag{2.25}$$

where the operator $\mathbb{P}$ can be taken as any projection into the piecewise polynomial space $\mathbb{V}_h^k$ as long as it is the same projection that was used to evaluate the numerical initial condition. The fluctuation part, $U^f_{h,j}$, is again defined as in (2.8). With this, the cell interface value of A_0 takes the form of

$$(A_0)^*_{h,j+\frac{1}{2}} = \max\left((A_0)^+_{h,j+\frac{1}{2}}, (A_0)^-_{h,j+\frac{1}{2}} \right), \tag{2.26}$$

and the modified cell interface values of A_h become

$$A^{*,-}_{h,j+\frac{1}{2}} = \max\left(\left(\hat{E}_j + \sqrt{(A_0)^*_{h,j+\frac{1}{2}}}\right)^2 + A^{f,-}_{h,j+\frac{1}{2}}, 0 \right),$$

$$A^{*,+}_{h,j+\frac{1}{2}} = \max\left(\left(\hat{E}_{j+1} + \sqrt{(A_0)^*_{h,j+\frac{1}{2}}}\right)^2 + A^{f,+}_{h,j+\frac{1}{2}}, 0 \right). \tag{2.27}$$

The definition of $U^{*,\pm}_{h,j+\frac{1}{2}}$, as well as the left and right fluxes $\hat{f}^l_{j+\frac{1}{2}}$, $\hat{f}^r_{j-\frac{1}{2}}$, are defined in the same way, as in (2.13). These well-balanced numerical fluxes are consistent with those for the living-man equilibrium which will be presented in Section 4.

Alternatively, one may also follow the approach in [16] by letting

$$\sqrt{(A_0)^*_{h,j+\frac{1}{2}}} = \max\left(\sqrt{(A_0)^+_{h,j+\frac{1}{2}}}, \sqrt{(A_0)^-_{h,j+\frac{1}{2}}} \right), \tag{2.28}$$

and then redefining A_h at the cell interfaces as

$$\sqrt{A^{*,-}_{h,j+\frac{1}{2}}} = \max\left(\sqrt{A^-_{h,j+\frac{1}{2}}} - \sqrt{(A_0)^-_{h,j+\frac{1}{2}}} + \sqrt{(A_0)^*_{h,j+\frac{1}{2}}}, 0 \right),$$

$$\sqrt{A^{*,+}_{h,j+\frac{1}{2}}} = \max\left(\sqrt{A^+_{h,j+\frac{1}{2}}} - \sqrt{(A_0)^+_{h,j+\frac{1}{2}}} + \sqrt{(A_0)^*_{h,j+\frac{1}{2}}}, 0 \right), \tag{2.29}$$

without involving U_h^e and U_h^f in the definition of the numerical fluxes.

As for the source term approximation, we note that the source term decomposition (2.16) still holds. While U^e and U^f are defined differently in this subsection, the decomposition approach presented in Subsection 2.2.2 can still be applied. Note that the direct numerical integration may not give well-balanced methods, as explained in Remark 2.2. This completes our description of well-balanced methods for the non-zero pressure man-at-eternal-rest steady state (1.5). One can show that the living-man well-balanced method in Section 4 can reduce to this man-at-eternal-rest well-balanced method. Furthermore, one can show (2.29) and (2.27) each simplify to (2.11) when $A = A_0$.

Proposition 2. *The DG scheme (2.6) for the blood flow system (1.3) with the non-zero pressure man-at-eternal-rest steady state (1.5) is well-balanced when paired with (2.29) or (2.27), the numerical fluxes (2.13), and the source term decomposition (2.16).*

The proof is similar to the zero-pressure case and is thus omitted here.

Remark 2.3. When the cross-sectional area at rest, A_0, is constant, the traditional DG scheme is recovered, i.e., the numerical fluxes reduce to standard flux and the source term approximation is simply zero. First, it is easy to observe that the source term approximation (2.18) reduces to exactly 0, since $(A_0)_h$ is constant. Second, we will show that the left and right numerical fluxes reduce to the original DG fluxes. When A_0 is constant, then $(A_0)^*_{h,j+\frac{1}{2}} = (A_0)^+_{h,j+\frac{1}{2}} = (A_0)^-_{h,j+\frac{1}{2}}$, so the calculation of $A_h^{*,\pm}$ by definitions (2.11), (2.29) or (2.27) reduces to

$$A^{*,\pm}_{h,j+\frac{1}{2}} = \max\left(A^{\pm}_{h,j+\frac{1}{2}}, 0 \right) = A^{\pm}_{h,j+\frac{1}{2}}. \tag{2.30}$$

More generally, we have that $U^{*,\pm}_{h,j+\frac{1}{2}} = U^{\pm}_{h,j+\frac{1}{2}}$. Therefore, by definition of the left and right fluxes, we obtain $\hat{f}^l_{j+\frac{1}{2}} = \hat{f}_{j+\frac{1}{2}}$ and $\hat{f}^r_{j-\frac{1}{2}} = \hat{f}_{j-\frac{1}{2}}$.

3. Numerical tests for the man-at-eternal-rest well-balanced method

In this section, we present some numerical examples by testing the well-balanced DG scheme designed for the man-at-eternal-rest steady state in Section 2. The third order TVD Runge-Kutta time discretization (2.4) is used in conjunction with piecewise quadratic polynomials ($k = 2$) in space, unless otherwise stated. The CFL number is taken to be 0.15.

3.1. Accuracy test

Our first numerical example tests the accuracy of our man-at-eternal-rest well-balanced scheme on a problem with smooth so-

Table 1
L^1 errors and convergence orders of the accuracy test in Section 3.1, using P^0, P^1 and P^2 piecewise polynomials and the man-at-eternal-rest well-balanced method. In each case, $k+1$ order of accuracy is achieved.

		$k=0$		$k=1$		$k=2$	
Variable	J	L^1 Error	Order	L^1 Error	Order	L^1 Error	Order
A	25	6.1718e-01		4.0986e-02		1.7291e-03	
	50	4.0692e-01	0.6009	1.0077e-02	2.0241	2.2503e-04	2.9418
	100	2.4564e-01	0.7282	2.5017e-03	2.0093	2.8740e-05	2.9690
	200	1.3642e-01	0.8485	6.2420e-04	2.0028	3.6297e-06	2.9851
	400	7.2062e-02	0.9207	1.5614e-04	1.9992	4.5768e-07	2.9874
Q	25	2.5275e02		6.2128e00		3.4189e-01	
	50	1.4833e02	0.7689	1.5283e00	2.0233	4.1757e-02	3.0334
	100	8.0719e01	0.8779	3.8083e-01	2.0047	5.1194e-03	3.0280
	200	4.2203e01	0.9356	9.5287e-02	1.9989	6.3175e-04	3.0185
	400	2.1582e01	0.9676	2.3935e-02	1.9931	7.8696e-05	3.0050

Table 2
Parameters in the initial condition (3.2) for the zero pressure man-at-eternal-rest well-balanced tests.

$\tilde{R}$	ΔR	K	ρ	x_1	x_2	x_3	x_4	L
$4\times10^{-3}m$	$10^{-3}m$	$10^8\ \frac{Pa}{m}$	$1060\ \frac{kg}{m^3}$	$10^{-2}m$	$3.05\times10^{-2}m$	$4.95\times10^{-2}m$	$7\times10^{-2}m$	$0.14m$

lutions. The initial conditions for $x \in [0, 10]$ are

$$A(x,0) = \sin\left(\frac{\pi}{5}x\right) + 10, \qquad Q(x,0) = e^{\cos(\frac{\pi}{5}x)}, \tag{3.1}$$

with the cross-sectional area at rest

$$A_0(x) = \frac{1}{2}\cos^2\left(\frac{\pi}{5}x\right) + 5,$$

and $K = 10^8\ \frac{Pa}{m}$, $\rho = 1060\ \frac{kg}{m^3}$. Periodic boundary conditions are employed. We compute until time $t = 0.01$ when the solution is still smooth. Since there is no explicitly known solution in this case, the errors are computed by iteratively comparing results from meshes of uniform cell widths h and $h/2$. Table 1 contains the L^1 errors and orders of accuracy for P^0, P^1 and P^2 polynomials. For each polynomial degree k, we see that $(k+1)^{\text{th}}$ order accuracy is achieved.

3.2. Tests for the well-balanced property

3.2.1. A zero pressure man-at-eternal-rest steady state

In this section, we demonstrate that the proposed DG scheme aptly preserves the zero pressure man-at-eternal-rest steady state (1.6) with a non-constant cross-sectional area at rest. We consider the case of a dead man with an aneurysm, which implies there is no blood flow occurring in a section of an artery that has a non-constant radius. An aneurysm occurs when the arterial wall weakens and balloons outwards. The initial conditions for the radius, R, are given by

$$R(x,0) = R_0(x)$$
$$= \begin{cases} \tilde{R}, & \text{if } x \in [0, x_1] \cup [x_4, L], \\ \tilde{R} + \frac{\Delta R}{2}\left[\sin\left(\frac{x-x_1}{x_2-x_1}\pi - \frac{\pi}{2}\right) + 1\right], & \text{if } x \in [x_1, x_2], \\ \tilde{R} + \Delta R, & \text{if } x \in [x_2, x_3], \\ \tilde{R} + \frac{\Delta R}{2}\left[\cos\left(\frac{x-x_3}{x_4-x_3}\pi\right) + 1\right], & \text{if } x \in [x_3, x_4], \end{cases} \tag{3.2}$$

for an artery of length L, with all the remaining parameters found in Table 2. The initial conditions for the cross-sectional area and cross-sectional area at rest are thus given by

$$A(x,0) = \pi R(x,0)^2, \qquad A_0(x) = \pi R_0(x)^2. \tag{3.3}$$

The initial velocity is assumed to be zero, thus $Q(x,0) = 0$. We impose transmissive boundary conditions at both endpoints of the domain and compute this example until time $t = 5$. Since the initial condition is the man-at-eternal-rest steady state, the solution should stay unchanged. The L^1 and L^∞ errors of the numerical solutions are shown in Table 3 and demonstrate that the well-balanced property was maintained when using the man-at-eternal-rest well-balanced scheme. The errors were computed by comparing the numerical solution to the numerical initial conditions. Fig. 2 shows the area of the artery and the velocity at $t = 5$ with a mesh of 200 cells.

For comparison, we also compute the same test using the traditional DG method in which the standard numerical fluxes are used

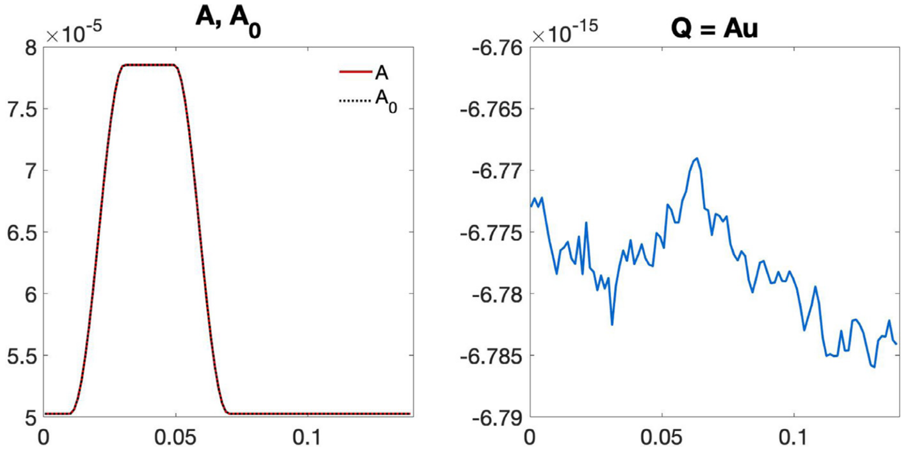

Fig. 2. Numerical solutions of the man-at-eternal-rest problem in Section 3.2, at time $t = 5$ with quadratic basis functions and mesh of size 200 uniform cells.

Table 3
Table of absolute and relative L^1 and L^∞ errors for the zero pressure man-at-eternal-rest well-balanced test representing an aneurysm in Section 3.2. Errors are given for both the traditional DG scheme and the well-balanced scheme. The well-balanced scheme demonstrates the well-balanced property, while the traditional DG scheme does not have the well-balanced property. Relative errors are included for A since the scale of the problem is so small. However, relative errors are not included for Q since the exact value is identically 0.

		Traditional DG Scheme		Man-at-Eternal-Rest WB DG Scheme	
Variable	Error Type	L^1 Error	L^∞ Error	L^1 Error	L^∞ Error
A	Absolute	1.8404e-13	1.7712e-08	2.042e-19	2.4335e-15
	Relative	3.3148e-09	3.1990e-04	3.5744e-15	3.8730e-11
Q	Absolute	1.8404e-13	1.7712e-08	2.042e-19	2.4335e-15

Table 4
Parameters in (3.4) for the non-zero pressure man-at-eternal-rest well-balanced tests.

$\tilde{R}$	ΔR	K	ρ	L	x_1	x_2	x_3	x_4
$4 \times 10^{-3} m$	$10^{-3} m$	$10^8 \ \frac{Pa}{m}$	$1060 \ \frac{kg}{m^3}$	$0.14 m$	$\frac{9L}{40}$	$\frac{1L}{4}$	$\frac{3L}{4}$	$\frac{31L}{40}$

and the source term is computed with a straightforward numerical integration. Fig. 3 and the errors in Table 3 demonstrate that the traditional DG scheme does not preserve the steady state exactly in the discrete level.

3.2.2. A non-zero pressure man-at-eternal-rest steady state

In this subsection, we consider the case of a dead man with stenosis. Stenosis occurs when the artery narrows and it leads to reduced blood flow from the heart to the rest of the body. Stenosis can be caused by a congenital heart defect, calcium buildup,or rheumatic fever which is a result of a strep throat infection. The radius at rest, R_0, for an artery of length L is given by

$$R_0(x) = \begin{cases} \tilde{R} + \Delta R, & \text{if } x \in [0, x_1] \cup [x_4, L], \\ \tilde{R} - \frac{\Delta R}{2}\left[\sin\left(\frac{x - x_1}{x_2 - x_1}\pi - \frac{\pi}{2}\right) - 1\right], & \text{if } x \in [x_1, x_2], \\ \tilde{R}, & \text{if } x \in [x_2, x_3], \\ \tilde{R} - \frac{\Delta R}{2}\left[\cos\left(\frac{x - x_3}{x_4 - x_3}\pi\right) - 1\right], & \text{if } x \in [x_3, x_4], \end{cases} \tag{3.4}$$

where all the parameters are found in Table 4.

Then the initial conditions are determined by the equilibrium values, that is

$$A(x, 0) = (C + \sqrt{\pi} R_0(x))^2, \qquad Q(x, 0) = 0. \tag{3.5}$$

where we set the constant $C = 10^{-3}$. We impose transmissive boundary conditions and run the scheme until the final time of $t = 1$ on mesh sizes of 50 and 200 uniform cells. The errors are found in Table 5 and demonstrate that the well-balanced property is preserved even on the coarse mesh of 50 cells. We also compare the results of the traditional DG scheme and non-zero pressure man-at-eternal-rest scheme well-balanced DG scheme in Fig. 4. It is clear from the figures that the use of a well-balanced scheme is especially important for preserving the non-constant area A.

3.3. Tests for small perturbations of the man-at-eternal-rest steady states

In this section, we examine multiple tests in which the initial conditions of a man-at-eternal-rest steady state are perturbed in a small region. The initial perturbation will split into two waves moving away from the source in opposite directions. We compare the man-at-eternal-rest well-balanced and traditional DG schemes to demonstrate the advantage of well-balanced methods in handling the propagation of these small perturbations.

Different wave propagation behaviors arise in arteries with constant and variable cross-sectional areas. We will first discuss the expected behaviors before exploring specific examples. Suppose an incident pulse is introduced at the left arterial end (with cross-sectional area A_1) and then travels towards the right (with cross-sectional area A_2). When the pulse crosses into the region of the vessel with cross-sectional area A_2 it generates a transmission pulse propagating in the same direction, and also a reflected pulse propagating to the left. The speed and wavelength of the reflected pulse is the same as the incident pulse because both pulses are traveling in the same medium. The amplitude of the reflected pulse is smaller and can be either inverted or non-inverted depending on the shape of the cross-sectional area. The reflection pulse is inverted when $A_1 < A_2$, and non-inverted when $A_1 > A_2$. See Fig. 5 for a visualization of this process. The ratio of the amplitude of

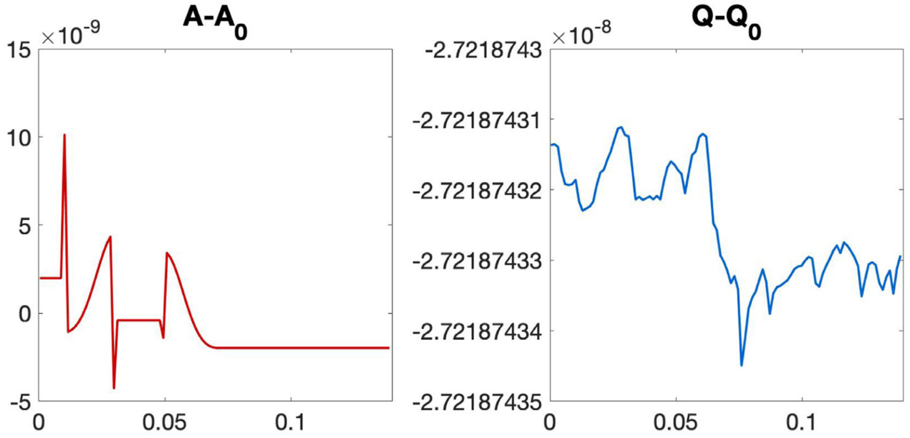

Fig. 3. The difference between A, Q at the final time $t = 5$ and the numerical initial conditions, when the traditional DG scheme is used for the man-at-eternal-rest problem in Section 3.2.

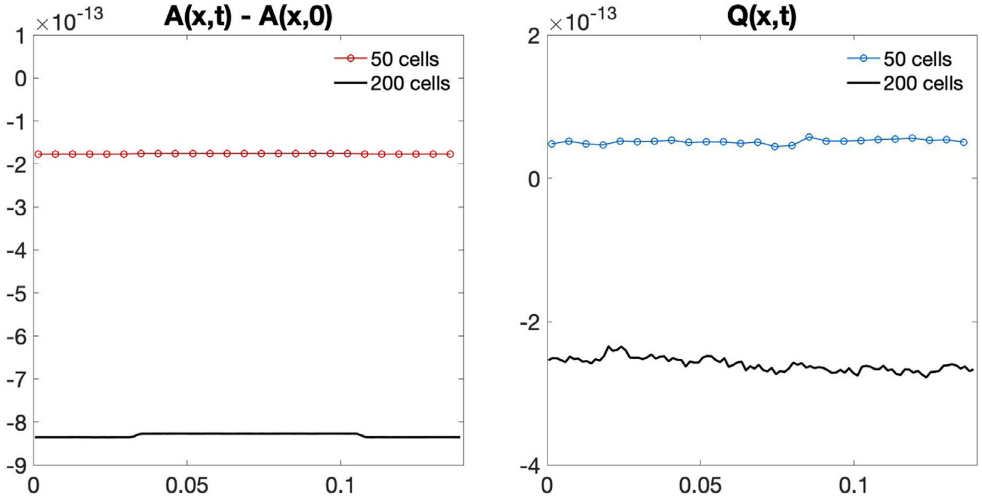

(a) Non-zero pressure man-at-eternal-rest well-balanced DG scheme

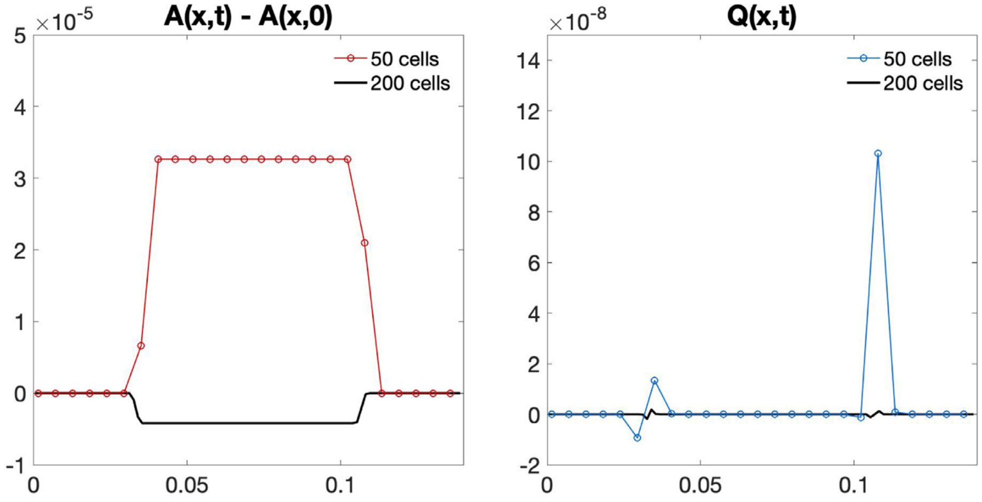

(b) Traditional DG scheme

Fig. 4. Plots of the errors at time $t = 1$ for the non-zero pressure man-at-eternal-rest problem from Section 3.2.2. The results using the non-zero pressure man-at-eternal-rest well-balanced scheme (top row) are compared with the results when using the traditional DG scheme (bottom row).

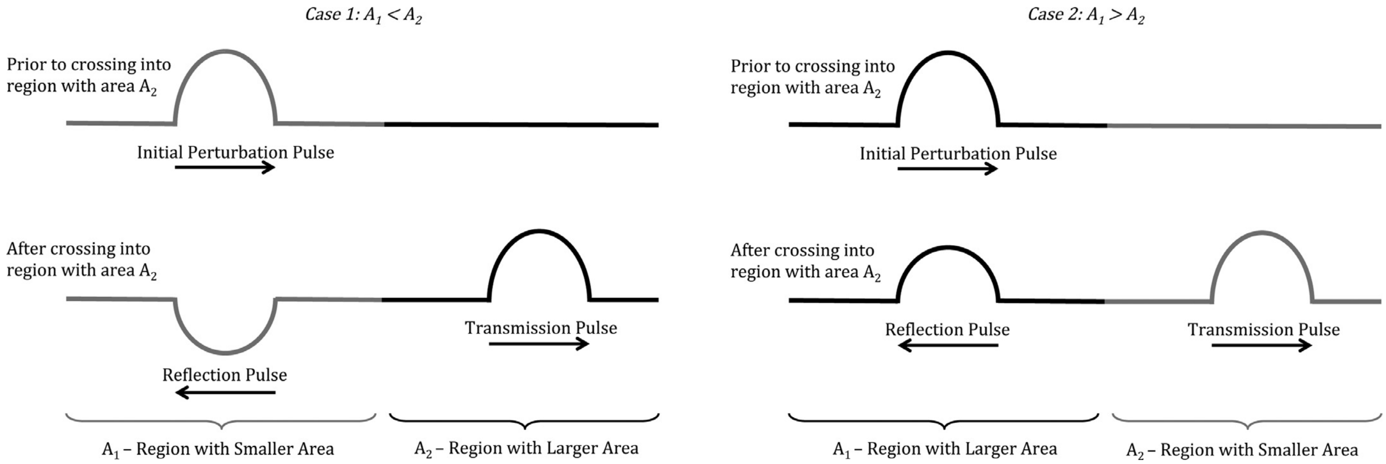

Fig. 5. An initial perturbation pulse splits into a transmission and reflection pulse when it moves from a region of area A_1 to a region of area A_2. The transmission pulse continues in the same direction of the original pulse while the reflection pulse moves in the opposite direction.

Table 5
Table of absolute and relative L^1 and L^∞ errors for non-zero pressure man-at-eternal-rest well-balanced test representing stenosis in Section 3.2.2. Errors are given for the traditional DG scheme and the well-balanced scheme for both $J = 50$ and $J = 200$ uniform spatial cells. The well-balanced scheme demonstrates the well-balanced property, while the traditional DG scheme does not have the well-balanced property.

			Traditional DG Scheme		Man-at-Eternal-Rest WB DG Scheme	
J	Variable	Error Type	L^1 Error	L^∞ Error	L^1 Error	L^∞ Error
50	A	Absolute	6.5745e-09	3.2637e-05	6.9075e-17	1.7727e-13
		Relative	2.0676e-07	1.0273e-03	2.1538e-15	5.5236e-12
	Q	Absolute	6.9733e-13	7.5473e-08	2.0062e-17	5.8616e-14
200	A	Absolute	2.1580e-10	4.1932e-06	8.1454e-17	8.3574e-13
		Relative	6.7907e-09	1.3198e-04	2.5398e-15	2.6044e-11
	Q	Absolute	2.1929e-15	1.3615e-09	2.5451e-17	2.7981e-13

Table 6
Parameters for the wave equation problem (3.7).

R_0	K	ρ	x_1	x_2	x_3	L	ϵ
$4 \times 10^{-3} m$	$10^8\ \frac{Pa}{m}$	$1060\ \frac{kg}{m^3}$	$\frac{2L}{10} m$	$\frac{4L}{10} m$	$\frac{6L}{10} m$	$0.16m$	5×10^{-3}

the reflected pulse and the incident pulse, known as the reflection coefficient $\mathcal{R}$, can be computed exactly and is given by

$$\mathcal{R} = \frac{\frac{A_1}{C_1} - \frac{A_2}{C_2}}{\frac{A_1}{C_1} + \frac{A_2}{C_2}}. \tag{3.6}$$

where the Moens–Korteweg coefficients C_i corresponding to A_1 and A_2 are defined as $C_i = \sqrt{\frac{K\sqrt{A_i}}{2\rho\sqrt{\pi}}}$ for $i = 1, 2$. The transmission coefficient, $\mathcal{T}$, given by $\mathcal{T} = 1 + \mathcal{R}$ represents the ratio of the amplitude of the transmission pulse to the incident pulse.

The numerical example in Section 3.3.1 portrays an artery with constant cross-sectional area. Therefore, the waves resulting from the perturbation will propagate through the domain and after they exit the domain, the radii will return to the unperturbed state. On the other hand, the examples in Sections 3.3.2 and 3.3.3 represent arteries with non-constant cross-sectional area, resulting in the appearance of reflection and transmission pulses.

3.3.1. Wave equation

We start with the following wave equation example with constant cross-section at rest, which has been studied in [8] by Delestre et al. It is a small perturbation test, in which an “approximate” solution can be found analytically. The initial conditions are given by

$$A(x,0) = \begin{cases} \pi (R_0)^2, & \text{if } x \in [0, x_2] \cup [x_3, L], \\ \pi (R_0)^2 \left[1 + \epsilon \sin\left(\pi \frac{x - x_2}{x_1}\right)\right]^2, & \text{if } x \in [x_2, x_3], \end{cases}$$
$$Q(x,0) = 0, \tag{3.7}$$

on the computational domain [0, L]. The cross-section at rest is given by $A_0(x) = \pi R_0(x)^2$. The parameters used in our simulation are listed in Table 6.

As shown in [8], when neglecting all the high order terms of ϵ, its solution can be expressed as

$$\begin{cases} R(x,t) = R_0 + \dfrac{\epsilon}{2}[\phi(x - C_0 t) + \phi(x + C_0 t)], \\ u(x,t) = -\epsilon \dfrac{C_0}{R_0}[-\phi(x - C_0 t) + \phi(x + C_0 t)], \end{cases} \tag{3.8}$$

where $\phi(x) = R_0 \sin(\pi \frac{x - x_2}{x_1}) \mathbb{1}_{[x_2, x_3]}$ with $\mathbb{1}$ being the indicator function and the constant C_0 is the Moens–Korteweg wave velocity

$$C_0 = \sqrt{\frac{K\sqrt{A_0}}{2\rho\sqrt{\pi}}} = \sqrt{\frac{KR_0}{2\rho}} \approx 13.73. \tag{3.9}$$

Table 7
Parameters for (3.10) in the propagation of a pulse to and from an expansion problems.

$\tilde{R}$	ΔR	K	ρ	x_1	x_2	L
$4 \times 10^{-3} m$	$10^{-3} m$	$10^8\ \frac{Pa}{m}$	$1060\ \frac{kg}{m^3}$	$\frac{19L}{40} m$	$\frac{L}{2} m$	$0.16m$

We employee transmissive boundary conditions at the endpoints of the domain. Fig. 6 shows the numerical results at times $t = 0.002, 0.004$, and 0.006 with a mesh of 200 cells. Comparison with the analytical exact solution (3.8) demonstrates that these small perturbations are well captured.

3.3.2. Propagation of a pulse to and from an expansion

In the examples below, we consider the reflection and the transmission of a small wave in an aneurysm, when the cross-section at rest is not a constant. Following the setup in [8], we consider the radius of the cross-section at rest given by

$$R_0(x) = \begin{cases} \tilde{R} + \Delta R, & \text{if } x \in [0, x_1], \\ \tilde{R} + \frac{\Delta R}{2}\left[1 + \cos\left(\frac{x - x_1}{x_2 - x_1}\pi\right)\right], & \text{if } x \in [x_1, x_2], \\ \tilde{R}, & \text{otherwise}, \end{cases} \tag{3.10}$$

where the necessary parameters are listed in Table 7.

First, we consider a pulse propagating towards an expansion. The perturbation is applied to the region of the artery with smaller radii and given by the following

$$R(x,0) = \begin{cases} R_0(x)\left[1 + \epsilon \sin\left(\dfrac{100}{20L}\pi\left(x - \dfrac{65L}{100}\right)\right)\right], & \text{if } x \in \left[\frac{65L}{100}, \frac{85L}{100}\right], \\ R_0(x), & \text{otherwise}. \end{cases} \tag{3.11}$$

The parameter $\epsilon = 5.0 \times 10^{-3}$ and the momentum $Q(x,0) = 0\ \frac{m^3}{s}$ are considered. The boundary conditions are transmissive at the endpoints of the domain. The initial state and numerical solutions at times $t = 0.002$ and $t = 0.006$ are presented in Fig. 7. Fig. 8 demonstrates how the wave propagates as a function of time for all time.

Second, we consider a pulse propagation from an expansion. In this case, the perturbation is initiated in the region of the vessel with larger area. The perturbed radius now becomes

$$R(x,0) = \begin{cases} R_0(x)\left[1 + \epsilon \sin\left(\dfrac{100}{20L}\pi\left(x - \dfrac{15L}{100}\right)\right)\right], & \text{if } x \in \left[\frac{15L}{100}, \frac{35L}{100}\right], \\ R_0(x), & \text{otherwise}, \end{cases} \tag{3.12}$$

where $\epsilon = 5.0 \times 10^{-3}$. As before, the fluid is at rest, $Q(x,0) = 0\ \frac{m^3}{s}$, and transmissive boundary conditions are imposed at the endpoints of the domain. In Fig. 9, we see the initial state and numer-

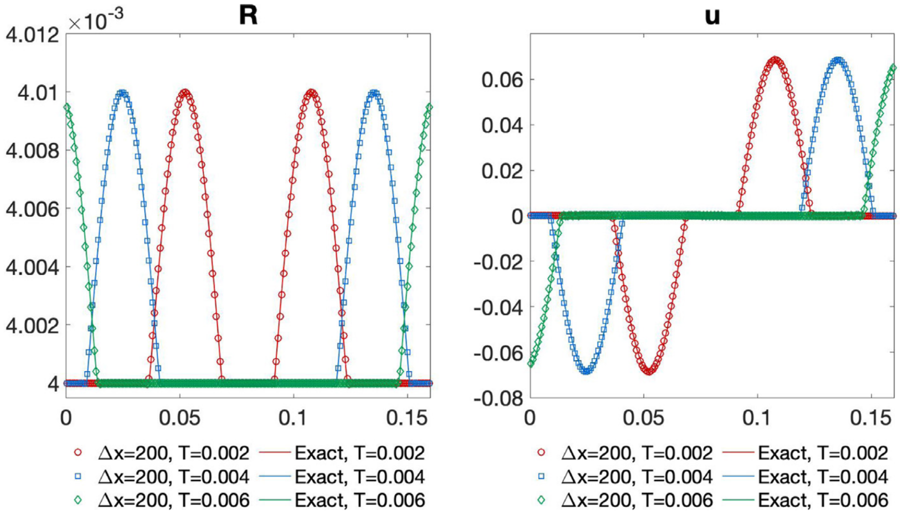

Fig. 6. Solutions of the radius R and velocity u of the wave equation problem at various times with quadratic basis functions and a uniform mesh of 200 cells and the exact solutions at the same times.

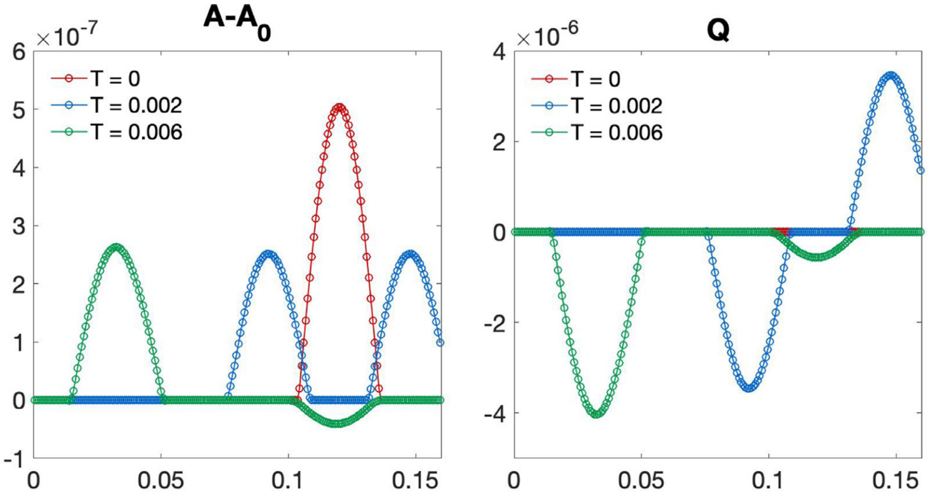

Fig. 7. Initial conditions and solution of the propagation of a pulse to an expansion problem at various times with a mesh of 200 uniform cells. The reflection pulse, visible at time $t = 0.006$, is inverted.

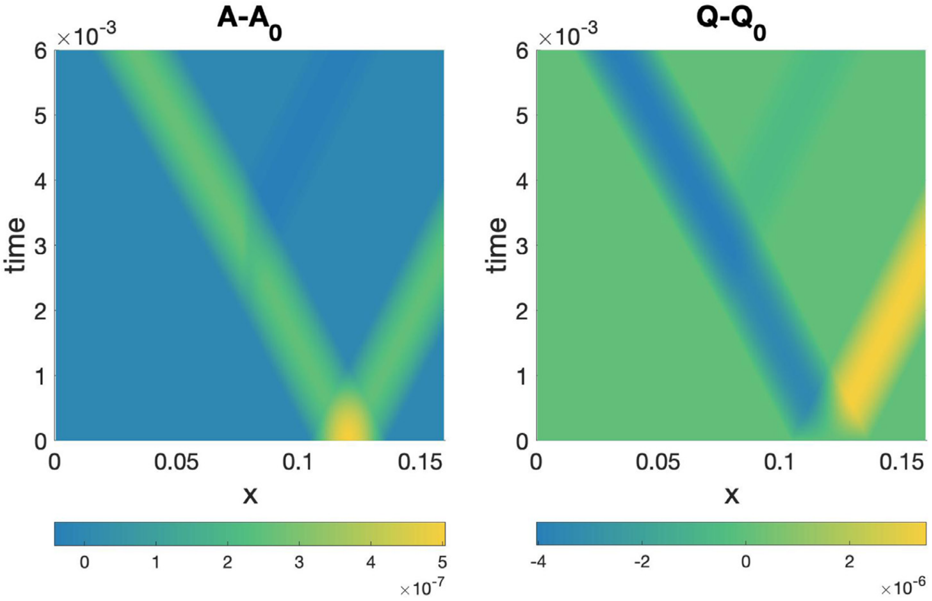

Fig. 8. Propagation of the pulse to an expansion over all time. The plots show the difference between the numerical solution at time t and the initial conditions. A mesh of 200 uniform cells was used to compute the solution. Around time $t = 0.003$ the left-moving wave meets the expansion and the inverted reflection wave forms.

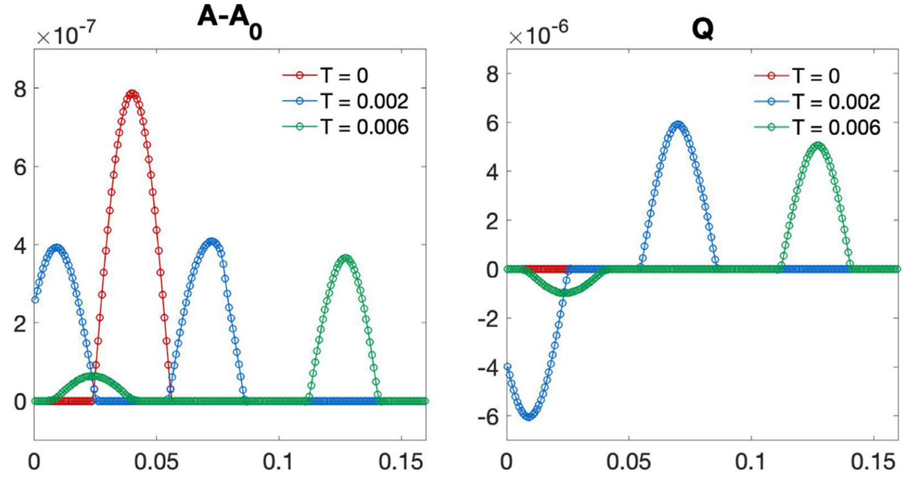

Fig. 9. Initial conditions and solution of the propagation of a pulse from an expansion problem at various times computed with a mesh of 200 uniform cells. The reflection pulse, visible at time $t = 0.006$, is non-inverted.

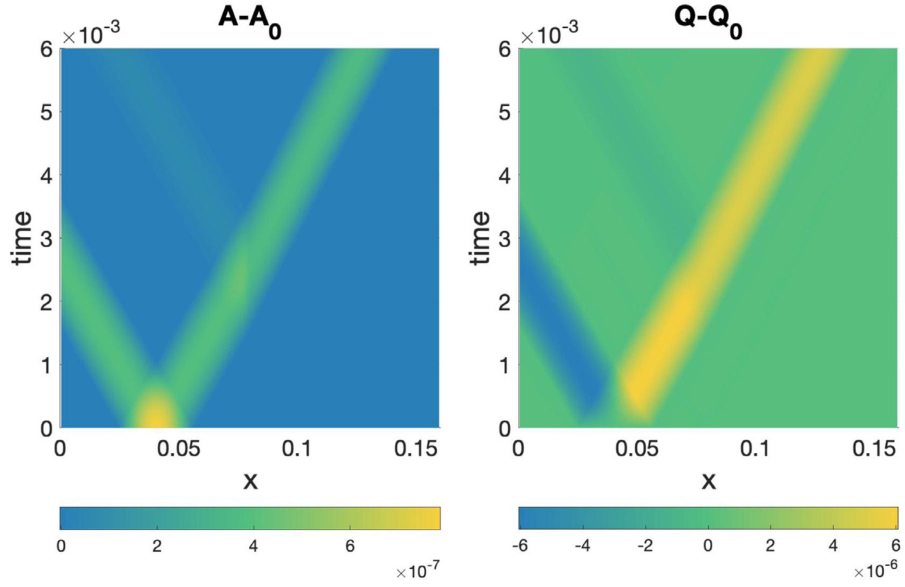

Fig. 10. Propagation of the pulse from an expansion over all time. The plots show the difference between the numerical solution at time t and the initial conditions. A mesh of 200 uniform cells was used to compute the solution. Around time $t = 0.003$ the right-moving wave meets the expansion and the non-inverted reflection wave forms.

ical results at times $t = 0.002$ and $t = 0.006$. Fig. 10 demonstrates how the wave propagates as a function of time for all time.

3.3.3. Perturbation of a non-zero pressure man-at-eternal-rest well-balanced problem

In this subsection, we impose a small perturbation to a non-zero pressure man-at-eternal-rest steady state problem representing stenosis in a ‘dead man’. We show that the well-balanced scheme aptly handles the perturbation. We also compute the same test using the traditional DG scheme and compare the results.

The radius at rest is given by (3.4) and the original initial conditions are given by (3.5). We impose a small perturbation at the center of the artery to the cross-sectional radii in the following manner,

$$R_{pert}(x,0) = \begin{cases} R_0(x)\left[1+\epsilon \sin\left(\frac{100}{10L}\pi\left(x-\frac{45L}{100}\right)\right)\right], & \text{if } x \in \left[\frac{45L}{100}, \frac{55L}{100}\right], \\ R_0(x), & \text{otherwise}. \end{cases}$$

The initial condition for the perturbed cross-sectional area is then defined as $A_{pert}(x,0) = \pi R_{pert}(x,0)^2$. The scheme is run until time $t = 8 \times 10^{-4}$, before the traveling perturbation waves exit the domain.

We test this problem with $\epsilon = 10^{-3}$ and $\epsilon = 10^{-4}$ for two different sizes of mesh, $J = 50$ and $J = 200$ uniform cells. The results for the well-balanced DG scheme are presented in Fig. 11 and the results for the traditional DG scheme are found in Fig. 12. The well-balanced scheme aptly handles the perturbation for either mesh size and for either size perturbation. On the other hand, the traditional DG scheme does not work as well. In the case where $J = 50$ uniform cells, then the undesirable behavior arises for either perturbation size. In the case where $J = 200$ uniform cells, the scheme has similar results for the perturbation with smaller amplitude (i.e. $\epsilon = 10^{-4}$), however the scheme improves when the amplitude of the perturbation is larger (i.e. $\epsilon = 10^{-3}$). However, in either case, the scheme is still out-performed by the well-balanced method.

4. Living-man well-balanced DG scheme

In this section, well-balanced methods for maintaining the general living-man steady state (1.7) will be described. Due to the

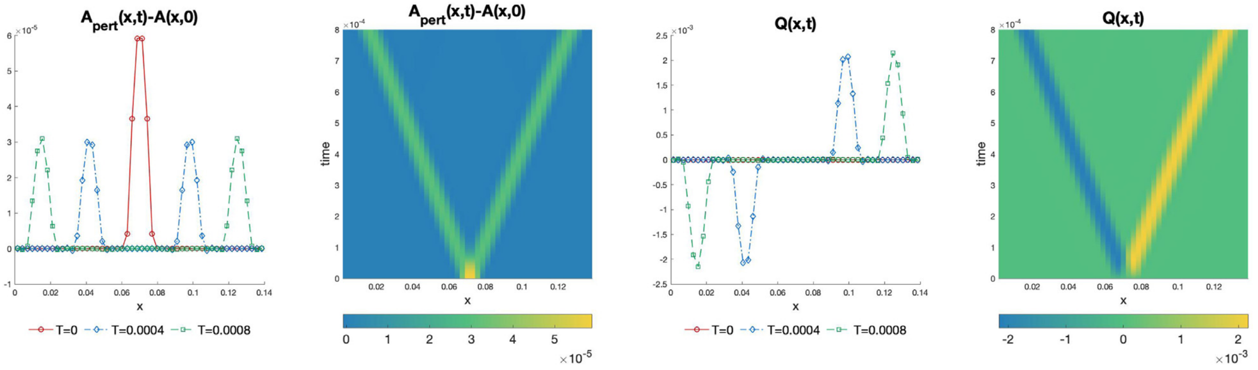

(a) $J = 50$ cells, $\epsilon = 10^{-3}$

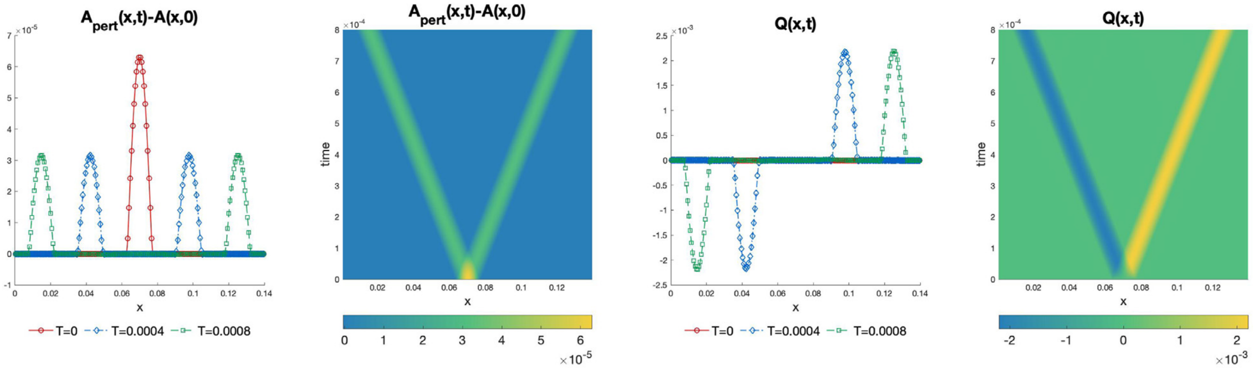

(b) $J = 200$ cells, $\epsilon = 10^{-3}$

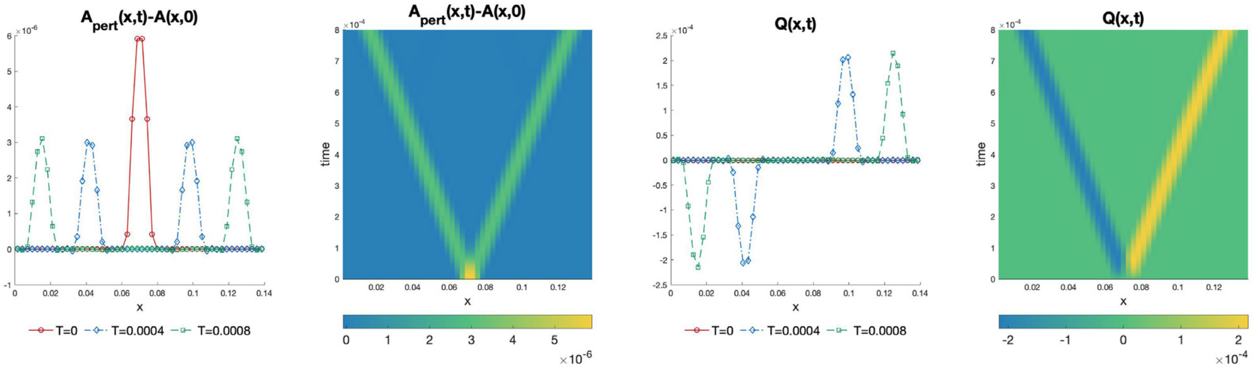

(c) $J = 50$ cells, $\epsilon = 10^{-4}$

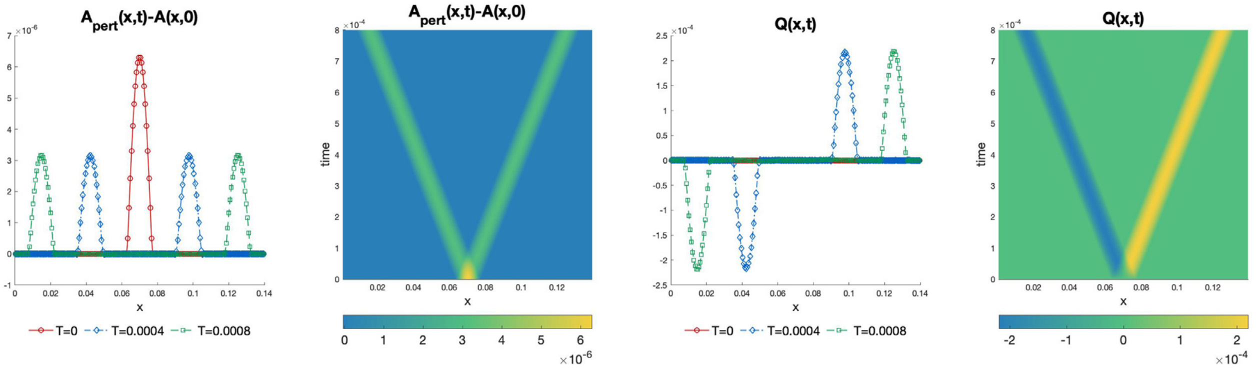

(d) $J = 200$ cells, $\epsilon = 10^{-4}$

Fig. 11. Perturbation of non-zero pressure man-at-eternal-rest well-balanced problem in Section 3.3.3 for all time up until $t = 0.008$ using the *non-zero pressure well-balanced DG scheme*. The scheme performs well for both mesh sizes and for both perturbation sizes.

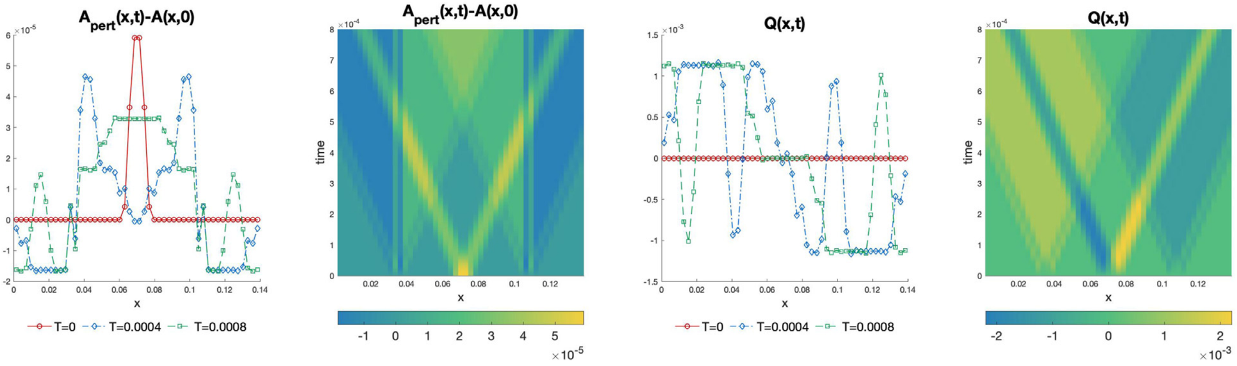

(a) $J = 50$ cells, $\epsilon = 10^{-3}$

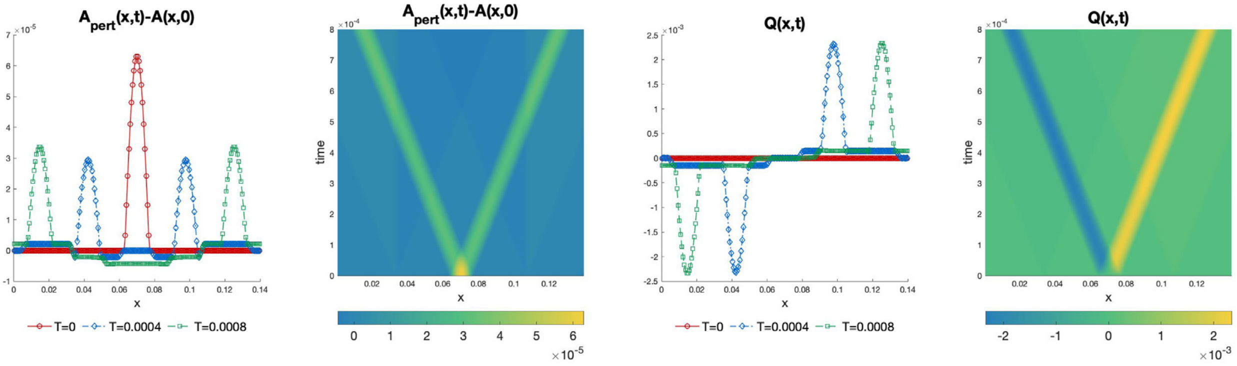

(b) $J = 200$ cells, $\epsilon = 10^{-3}$

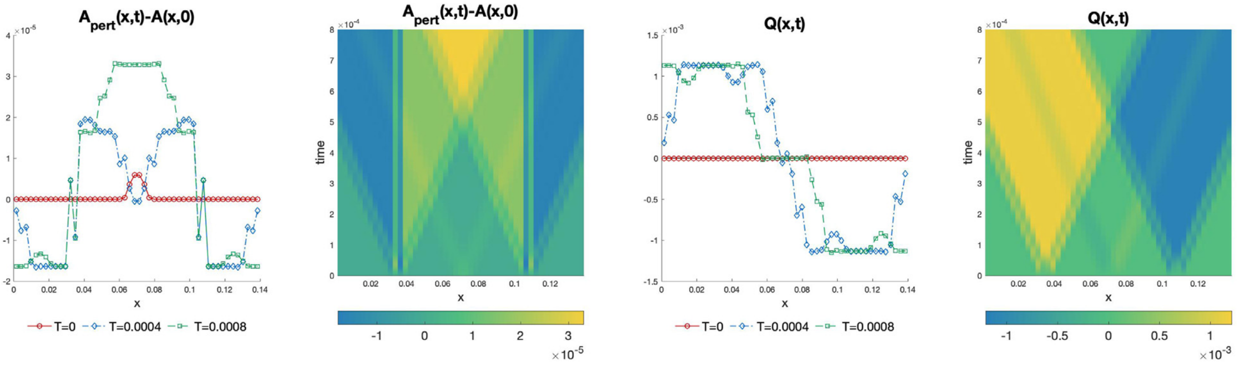

(c) $J = 50$ cells, $\epsilon = 10^{-4}$

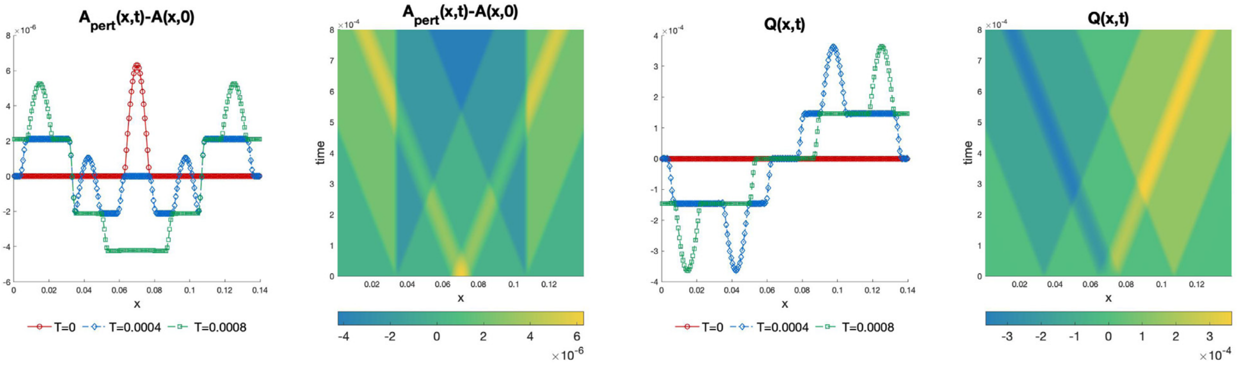

(d) $J = 200$ cells, $\epsilon = 10^{-4}$

Fig. 12. Perturbation of non-zero pressure man-at-eternal-rest well-balanced problem in Section 3.3.3 for all time up until $t = 0.008$ using the *traditional DG scheme*. The scheme performs poorly on the coarse mesh of 50 uniform cells for either size perturbation. For the refined mesh of 200 uniform cells, the scheme improves slightly for the larger perturbation, but still does not perform as well as the well-balanced scheme.

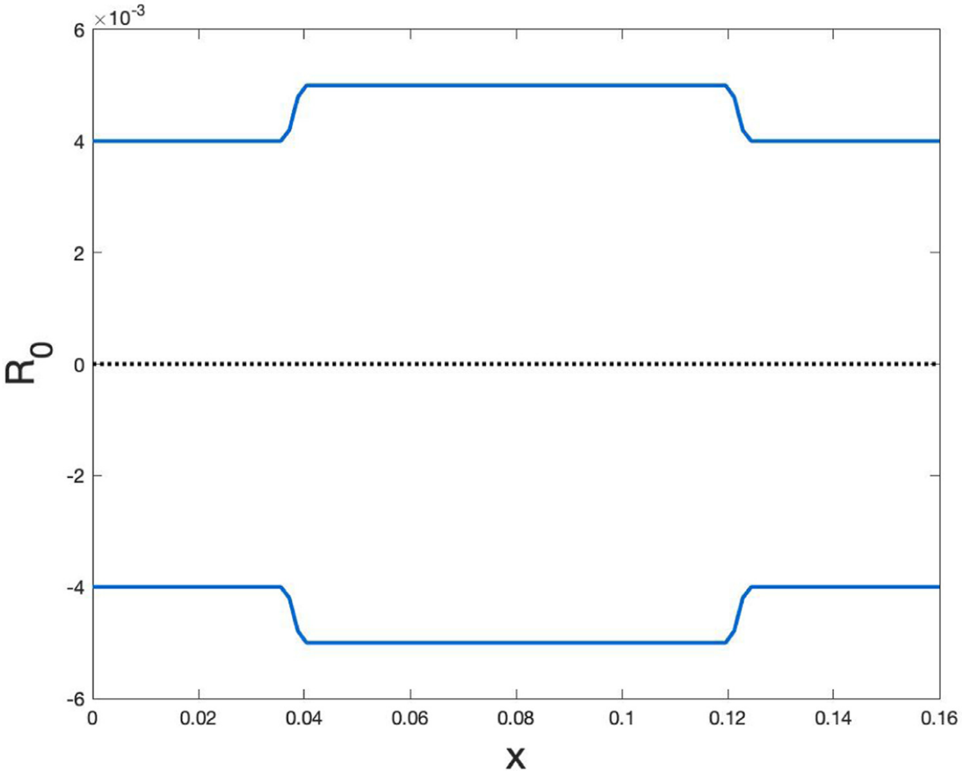

Fig. 13. Radii at rest for the artery with an aneurysm defined by (5.6).

complexity of the steady state, extra attention is given to the projection of the initial conditions, as well as the source term and numerical flux calculations.

4.1. Numerical initial conditions

In general, the L^2 projection of the true initial condition U_0 is taken to be the numerical initial condition U_h^0 for modal DG schemes, as was done for the man-at-eternal-rest well-balanced DG scheme in Section 2. However, the projected polynomial U_h^0 may not be in the equilibrium state. Thus the cell boundary values $U_{h,j+\frac{1}{2}}^{\pm}$, as well as the function values at the quadrature points used to evaluate the volume integral, may also not be in equilibrium. This contributes to the challenges of how to recover the equilibrium information from these polynomials. We would like to comment that this difficulty disappears for the finite difference methods, because the points values of the initial condition in any finite difference methods, by design, automatically satisfy the equilibrium.

The same difficulty also appears in high order well-balanced finite volume methods, whose numerical initial condition is simply the cell average. In [22] where well-balanced methods were designed for the shallow water equations with moving-water equilibrium state, this difficulty was identified. The issue was addressed in that paper by defining the well-balanced states as the solutions of nonlinear equations and then solving them using Newton's method. The same idea was later extended to construct numerical initial conditions of well-balanced DG methods in [33]. A simpler approach, without involving the nonlinear equations and the Newton's method, is proposed in [17], by introducing a special projection of the initial condition to take advantage of the flexibility of the DG method. A further modification of the projection from [17] is proposed in this paper to produce the numerical initial condition U_h^0.

We introduce the following projection $\mathbb{P}_h\omega$ of any function ω into the space $\mathbb{V}_h^k$ satisfying, on each interval I_j,

$$\int_{I_j} \mathbb{P}_h\omega v \, dx = \int_{I_j} \omega v \, dx, \tag{4.1}$$

for any $v \in P^{k-1}$ on I_j, and

$$(\mathbb{P}_h\omega)\left(x_{j+\frac{1}{2}}^-\right) = \omega\left(x_{j+\frac{1}{2}}^-\right), \tag{4.2}$$

at the right boundary value $x_{j+\frac{1}{2}}$ of the cell I_j. This projection is known as the Radau projection. The polynomial $\mathbb{P}_h\omega$ for each cell I_j can be determined by solving a local linear algebra problem of the size $(k+1)\times(k+1)$ derived from the discretized versions of (4.1) and (4.2). This is a local projection defined on each interval I_j. One can show that the error of this projection has optimal order of h^{k+1}.

The projections of the initial condition U_h^0 and the cross-sectional area at rest $(A_0)_h(x)$ are defined to be

$$U_h^0(x) = \mathbb{P}_h U_0(x), \quad (A_0)_h(x) = \mathbb{P}_h A_0(x). \tag{4.3}$$

At the right boundary point of each cell, it can be shown that

$$U_h^0\left(x_{j+\frac{1}{2}}^-\right) = U_0\left(x_{j+\frac{1}{2}}^-\right), \quad (A_0)_h\left(x_{j+\frac{1}{2}}^-\right) = A_0\left(x_{j+\frac{1}{2}}^-\right), \quad \text{for all } j, \tag{4.4}$$

which means that the equilibrium states (4.6) are recovered at these points

$$\left(\frac{u_h^2}{2} + \beta\left(\sqrt{A_h} - \sqrt{(A_0)_h}\right)\right)\left(x_{j+\frac{1}{2}}^-\right) = constant, \qquad \text{for all } j.$$

This information will be very useful when decomposing the solutions into the equilibrium and fluctuation parts in the following section.

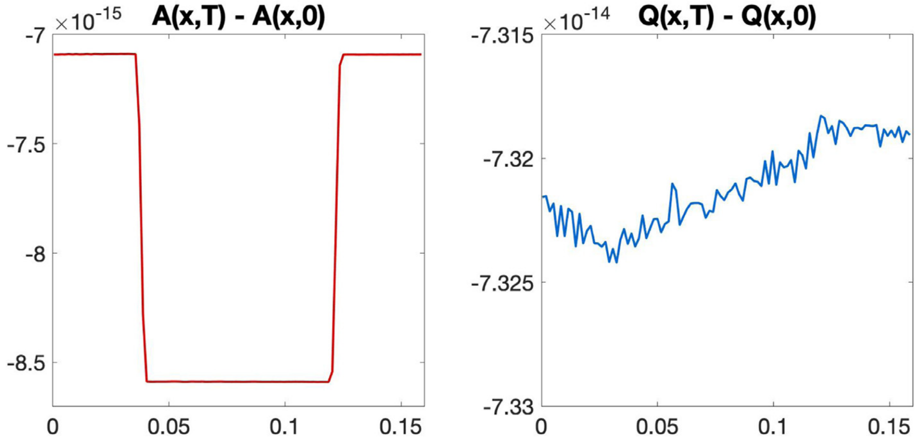

(a) Living-man well-balanced DG scheme

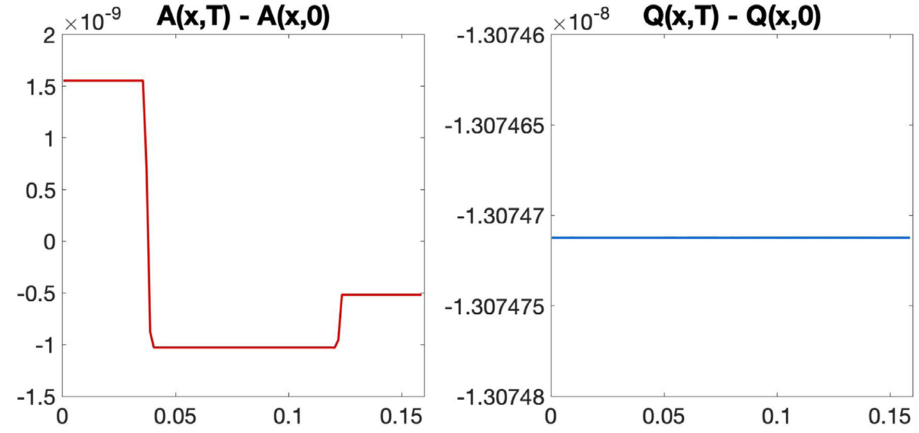

(b) Non-zero pressure man-at-eternal-rest well-balanced DG scheme

Fig. 14. The difference between A, Q at the final time $t = 5$ and the corresponding numerical initial conditions for the artery with an aneurysm problem from Section 5.2.1. We compare the living-man well-balanced DG method (top row) and the man-at-eternal-rest well-balanced DG method (bottom row). Both plots were computed with a mesh of 200 uniform cells and $S_{in} = 0.5$. The man-at-eternal-rest method does not handle the non-zero velocity equilibria as well as the living-man scheme.

Remark 4.1. In [17], a slightly different projection was introduced to compute the numerical initial conditions. That was defined by the formula (4.1), combined with

$$(\mathbb{P}_h\omega)(x_j) = \omega(x_j), \tag{4.5}$$

which requires the projected polynomial overlaps with the original function at the center x_j of each cell I_j. However, this projection may not be optimal for some polynomial degree k, therefore we introduce a different projection $\mathbb{P}_h$ in this paper. Note that the choice of this projection is not unique. Alternatively, we could have also chosen to fix the numerical initial conditions to be equal to the true solution at the left side of each computational cell.

4.2. Conservative, equilibrium variables and the decomposition of solutions

The living-man equilibrium variables from (1.7) will be denoted as

$$V = \begin{pmatrix} Q \\ E \end{pmatrix} = \begin{pmatrix} Q \\ \frac{Q^2}{2A^2} + \beta\left(\sqrt{A} - \sqrt{A_0}\right) \end{pmatrix}. \tag{4.6}$$

We need to transform the conservative variables U to the equilibrium variables V and vice versa, during the construction of well-balanced numerical flux. The equilibrium variables can be easily computed from U and the cross-sectional area at rest A_0, and we denote it by $V = V(U, A_0)$. On the other hand, suppose V and the cross-sectional area at rest A_0 are given, we can evaluate $U = U(V, A_0)$ (or simply $A = A(V, A_0)$ as Q can be directly obtained from V) in the following way. The equilibrium variable E is defined as

$$E = \frac{Q^2}{2A^2} + \beta\left(\sqrt{A} - \sqrt{A_0}\right),$$

which is equivalent to

$$\beta A^{\frac{5}{2}} - \left(\beta\sqrt{A_0} + E\right)A^2 + \frac{1}{2}Q^2 = 0. \tag{4.7}$$

The conservative variable A can be recovered by finding the root of the Eq. (4.7). One can use Newton's method to find the root, by using $A_h(x_i)$ as the initial guess, where x_i is either a quadrature point or a cell-boundary value depending on where we are solving the problem. Müller et al. [20] address the recovery of A from the living-man equilibrium by solving the similar nonlinear equation and considering the subcritical, supercritical, or critical cases. In [14] by Ghigo et al., they assume that values for Q are small enough that living-man equilibrium variables (1.7) can be approximated by (1.5). This eliminates the need to recover A from a fractional-degree equality.

Next, we propose the decomposition of the solution U_h into the reference equilibrium state U_h^e and the fluctuation state U_h^f. The

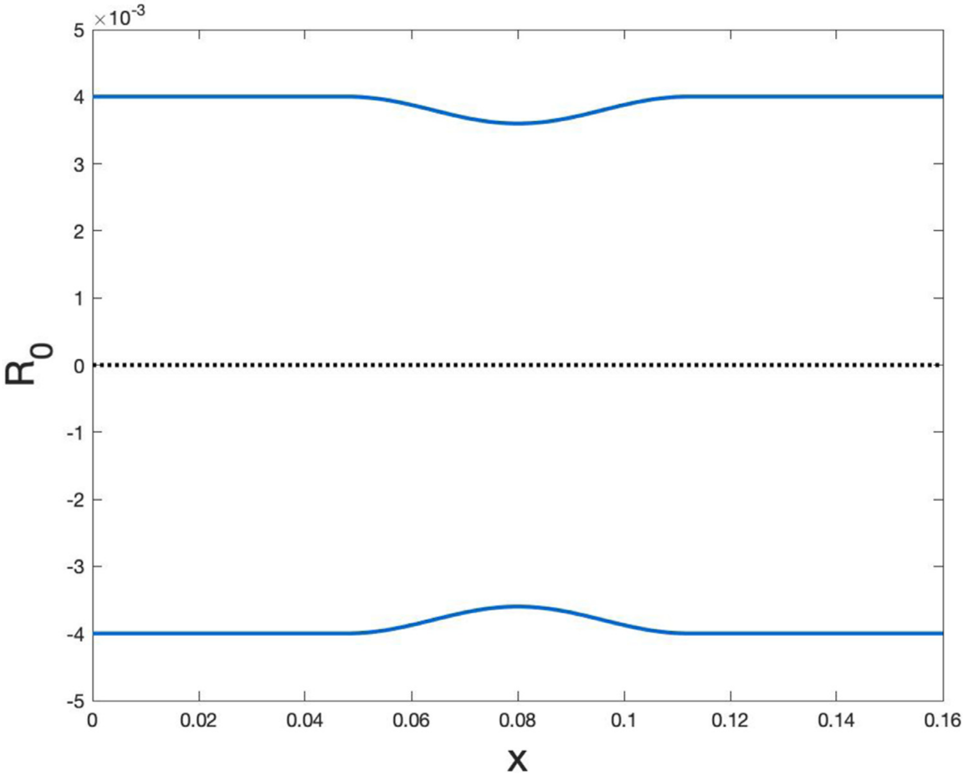

Fig. 15. Radii at rest for the artery with stenosis defined by (5.7).

reference equilibrium values $\hat{V}_j$ in cell I_j are defined as

$$\hat{V}_j = \begin{pmatrix} \hat{Q}_j \\ \hat{E}_j \end{pmatrix} = \begin{pmatrix} Q_h\left(x^-_{j+\frac{1}{2}}\right) \\ E_h\left(x^-_{j+\frac{1}{2}}\right) \end{pmatrix}. \tag{4.8}$$

The equilibrium state $U^e_h(x)$ can then be computed from these values and the true function $A_0(x)$ (not $(A_0)_h(x)$)

$$U^e_{h,j}(x) = \begin{pmatrix} A^e_{h,j}(x) \\ Q^e_{h,j}(x) \end{pmatrix} = \mathbb{P}_h U\left(\hat{V}_j, A_0(x)\right), \tag{4.9}$$

in each cell I_j. The projection $\mathbb{P}_h$ is used to ensure that $U^e_h \in \mathbb{V}^k_h$, since the functions $U\left(\hat{V}_j, A_0(x)\right)$ may no longer be piecewise polynomials due to the nonlinear mapping. Finally, we can decompose the numerical solution U_h as

$$U_h = U^e_h + U^f_h \tag{4.10}$$

with the fluctuation part $U^f_h = U_h - U^e_h \in \mathbb{V}^k_h$. Note that this decomposition will be computed at each time step t^n. Both U^e_h and U^f_h will be used in the computation of the well-balanced fluxes and source term approximations.

4.3. Well-balanced numerical fluxes

As explained in Section 2, the well-balanced DG scheme takes the form of

$$\int_{I_j} \partial_t U^n_h v\, dx - \int_{I_j} f(U^n_h)\partial_x v\, dx + \hat{f}^l_{j+\frac{1}{2}} v^-_{j+\frac{1}{2}} - \hat{f}^r_{j-\frac{1}{2}} v^+_{j-\frac{1}{2}} = \int_{I_j} S(U^n_h, (A_0)_h) v\, dx. \tag{4.11}$$

However, to achieve living-man well-balanced method, different ways to construct the well-balanced numerical flux and source term from those in Section 2 are needed.

If the system is in the living-man equilibrium (4.6), at the initial time t^0, the cell boundary values $U^-_{h,j+\frac{1}{2}}$ are equal to the exact equilibrium solutions at the right boundary point due to the choice of projection $\mathbb{P}_h$ (4.2), however the same does not hold for the other cell boundary values. This may generate discontinuous cell interface values, leading to non-well-balanced numerical fluxes, which may result in the equilibrium state not being preserved. One way to address this problem is to modify the projection so that the exact values are taken at both cell boundaries, with an example being the nodal DG method with Gauss–Lobatto nodes. Here, we would like to avoid the usage of Gauss–Lobatto nodes, and use the idea of hydrostatic reconstruction to determine the numerical fluxes, following the study in [33,35,39] in the context of the shallow water equations.

Prior to redefining the boundary values and constructing our fluxes, we first define the unique cell interface value of A_0 as

$$(A_0)^*_{h,j+\frac{1}{2}} = \max\left((A_0)^+_{h,j+\frac{1}{2}}, (A_0)^-_{h,j+\frac{1}{2}}\right), \tag{4.12}$$

for all j. This choice of $(A_0)^*_{h,j+\frac{1}{2}}$ will aid in guaranteeing continuity across the cell interface at the equilibrium state for the conservative variables. Now we set the redefined boundary values to be

$$\begin{aligned} U^{*,\pm}_{h,j+\frac{1}{2}} = \begin{pmatrix} A^{*,\pm}_{h,j+\frac{1}{2}} \\ Q^{*,\pm}_{h,j+\frac{1}{2}} \end{pmatrix} &= \begin{pmatrix} \max\left(0, A(\hat{V}_j, (A_0)^*_{h,j+\frac{1}{2}})\right) \\ \hat{Q}^\pm_{h,j+\frac{1}{2}} \end{pmatrix} + U^f_h(x^\pm_{j+\frac{1}{2}}) \\ &= \begin{pmatrix} \max\left(0, A(\hat{V}_j, (A_0)^*_{h,j+\frac{1}{2}})\right) + A^f_h(x^\pm_{j+\frac{1}{2}}) \\ Q^\pm_{h,j+\frac{1}{2}} \end{pmatrix}, \end{aligned} \tag{4.13}$$

where the values $\hat{V}_j$ are given in (4.8) and U^f_h is given in (4.10). When the system is in equilibrium, $A^f_h(x^\pm_{j+\frac{1}{2}}) = 0$ and $\hat{V}_j = \hat{V}_{j+1}$, hence $U^{*,-}_{h,j+\frac{1}{2}} = U^{*,+}_{h,j+\frac{1}{2}}$ for all j.

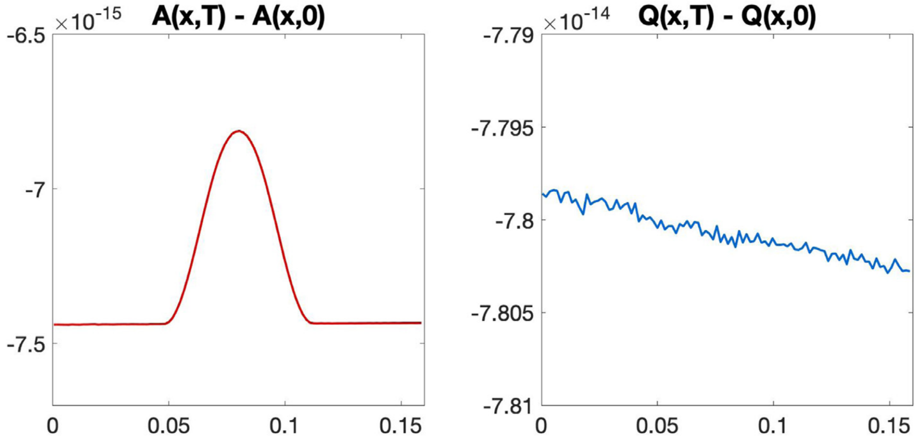

(a) Living-man well-balanced DG scheme

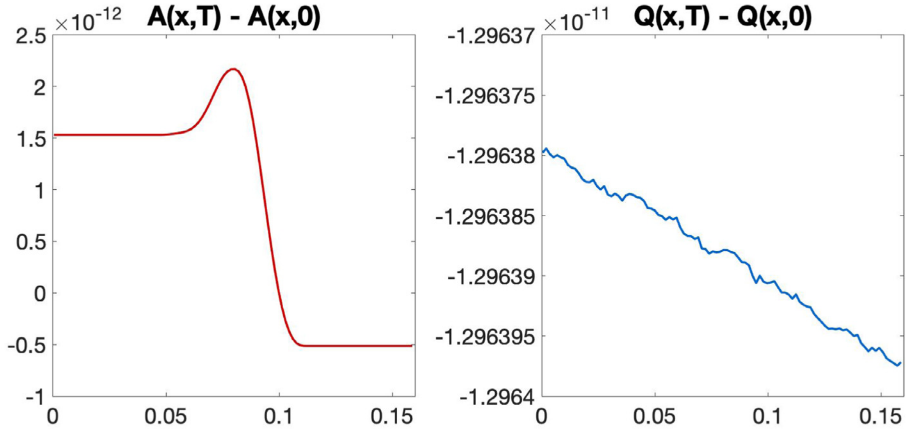

(b) Non-zero pressure man-at-eternal-rest well-balanced DG scheme

Fig. 16. The difference between A, Q at the final time $t = 5$ and the corresponding numerical initial conditions for the artery with stenosis problem from Section 5.2.2, when using the living-man well-balanced DG method (top row) and the man-at-eternal-rest well-balanced DG method (bottom row). Both plots were computed with a mesh of 200 uniform cells and $S_{in} = 0.5$.

It would also be satisfactory to define $(A_0)^*_{h,j+\frac{1}{2}} = \min((A_0)^+_{h,j+\frac{1}{2}}, (A_0)^-_{h,j+\frac{1}{2}})$, or other combinations of $(A_0)^\pm_{h,j+\frac{1}{2}}$ following the generalization of the hydrostatic reconstruction idea and designed to ensure continuity across the cell interfaces. One possible choice is to let $(A_0)^*_{h,j+\frac{1}{2}} = (A_0)^-_{h,j+\frac{1}{2}}$, then one can show that $A\left(\hat{V}_j, (A_0)^*_{h,j+\frac{1}{2}}\right) = A^-_{h,j+\frac{1}{2}}$ which eliminates the need to employ Newton's method to recover A.

Lastly, the well-balanced numerical fluxes can be computed in the same way as was introduced for the man-at-eternal-rest well-balanced scheme

$$\begin{aligned}\hat{f}^l_{j+\frac{1}{2}} &= F\left(U^{*,-}_{h,j+\frac{1}{2}}, U^{*,+}_{h,j+\frac{1}{2}}\right) + f\left(U^-_{h,j+\frac{1}{2}}\right) - f\left(U^{*,-}_{h,j+\frac{1}{2}}\right),\\ \hat{f}^r_{j-\frac{1}{2}} &= F\left(U^{*,-}_{h,j-\frac{1}{2}}, U^{*,+}_{h,j-\frac{1}{2}}\right) + f\left(U^+_{h,j-\frac{1}{2}}\right) - f\left(U^{*,+}_{h,j-\frac{1}{2}}\right),\end{aligned} \tag{4.14}$$

where $F(a, b)$ is a numerical flux, such as the Lax-Friedrichs flux defined in (2.3). Notice that when $U^{*,+}_{h,j+\frac{1}{2}} = U^{*,-}_{h,j+\frac{1}{2}}$, the fluxes reduce to

$$\hat{f}^l_{j+\frac{1}{2}} = f(U^-_{h,j+\frac{1}{2}}), \qquad \hat{f}^r_{j-\frac{1}{2}} = f(U^+_{h,j-\frac{1}{2}}) \tag{4.15}$$

as a result of the numerical flux $F(a, b)$ being consistent.

4.4. Well-balanced source term decomposition

The source term approximation for the living-man well-balanced scheme is approached in the same manner as in Section 2.2.2 for the man-at-eternal-rest well-balanced scheme. Due to the fact that the source term is linear with respect to the variable A, the source term can take on a decomposition similar to the form found in (4.10)

$$\int S(U_h, (A_0)_h)\nu\, dx = \int S(U^e_h, (A_0)_h)\nu\, dx + \int S(U^f_h, (A_0)_h)\nu\, dx. \tag{4.16}$$

The second term on the right hand side can be directly computed by any quadrature rule with sufficient accuracy. Since U^e_h is the equilibrium state, we can follow the discussion in Section 2.2.2 to approximate the first term. Thus the approximation for the source term takes the form

$$\begin{aligned}\int_{I_j} S(U_h, (A_0)_h)\nu\, dx = &-\int_{I_j} f(U^e_h)\nu_x\, dx + f(U^{e,-}_{h,j+\frac{1}{2}})\nu^-_{j+\frac{1}{2}}\\ &- f(U^{e,+}_{h,j-\frac{1}{2}})\nu^+_{j-\frac{1}{2}} + \int_{I_j} S(U^f_h, (A_0)_h)\nu\, dx.\end{aligned} \tag{4.17}$$

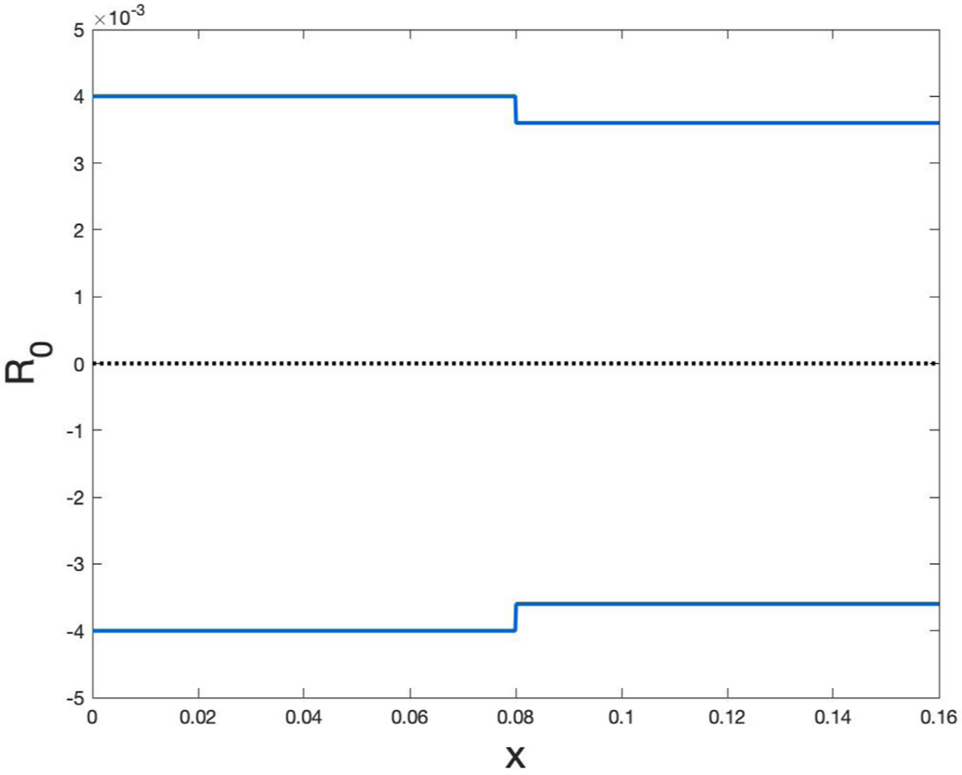

Fig. 17. Radii at rest for the artery with a decreasing step defined by (5.8).

The details of the derivation and some explanations can be found in Section 2.2.2.

4.5. A TVB slope limiter

In this section we discuss the implementation of a slope limiter, which is necessary when the solution contains discontinuities. We employ the modified minmod slope limiter with a total variation bounded (TVB) parameter M, defined as

$$\tilde{m}(a_1, \dots, a_l) = \begin{cases} a_1, & \text{if } |a_1| \le M\Delta x^2, \\ \text{minmod}(a_1, \dots, a_l), & \text{otherwise}, \end{cases} \tag{4.18}$$

with the minmod function given by

$$\text{minmod}(a_1, \dots, a_l) = \begin{cases} s\min(|a_1|, \dots, |a_l|), & \text{if } s = \text{sign}(a_1) = \dots = \text{sign}(a_l), \\ 0, & \text{otherwise} . \end{cases} \tag{4.19}$$

At each cell I_j, we define the modified cell boundary values to be

$$\begin{aligned} U_h^{(\text{mod})}(x^-_{j+\frac12}) &= \bar{U}_{h,j} \\ &+ \text{minmod}\Big(U_h(x^-_{j+\frac12}) - \bar{U}_{h,j}, \bar{U}^n_{h,j} - \bar{U}^n_{h,j-1}, \bar{U}^n_{h,j+1} - \bar{U}^n_{h,j}\Big), \\ U_h^{(\text{mod})}(x^+_{j-\frac12}) &= \bar{U}_{h,j} \\ &- \text{minmod}\Big(\bar{U}_{h,j} - U_h(x^+_{j-\frac12}), \bar{U}^n_{h,j} - \bar{U}^n_{h,j-1}, \bar{U}^n_{h,j+1} - \bar{U}^n_{h,j}\Big), \end{aligned} \tag{4.20}$$

where $\bar{U}^n_j$ is the cell average in cell I_j at time t^n. Note that the slope limiting procedure may not be required in every cell. If $\tilde{m}(a_1, \dots, a_l) = a_1$ (i.e., $U_h^{(\text{mod})}(x^\pm_{j\mp\frac12}) = U_h(x^\pm_{j\mp\frac12})$) in cell I_j, which implies that the solution is smooth, then limiting is not necessary in that cell. Otherwise, limiting is required and we can recover a new P^k polynomial $U^n_{h,j}(x)$ from the cell average $\bar{U}^n_{h,j}$ and the updated cell boundary values (4.20) for $k \ge 2$ that preserves the original cell average in I_j. This new polynomial then replaces the old one in this cell and will be used in the computation.

Note that when the living-man equilibrium state (1.7) is reached, the equilibrium may not be preserved if the slope limiter is activated. Therefore we wish to carefully determine which cells need limiting by applying the above procedure to the fluctuation part of the variables U_h^f. If limiting is required in a cell, the slope limiting procedure is then performed on U_h. Recall that when a steady state is reached, $U^f_{h,j} = 0$ for all values of j. Therefore, limiting is not required and the limiter has no affect on the well-balanced property.

It is important to note this procedure meets the necessary conditions of a limiter: it does not change the solution in smooth and well-balanced regions, and it does not change cell averages (hence maintains the mass conservation property of the DG method).

4.6. Verification of the living-man well-balanced property

Proposition 3. *The proposed RKDG scheme (2.6) with numerical fluxes (4.14) and source term approximation (4.17) is exactly well-balanced for the living-man equilibrium (1.7).*

Proof. We assume the initial data are in the living-man equilibria state, and the same analysis applies when the solution reaches the living-man equilibria at the time step t^n. The projection $\mathbb{P}_h$ guarantees the numerical initial conditions will satisfy the equilibrium condition at the values $x^-_{j+\frac12}$ for all j. This implies that $\hat{V}_j = constant$ for all j. Therefore, the equilibrium part, U_h^e, computed from $\hat{V}_j$ and $A_0(x)$ is equivalent to the conservative variable U_h, and this further implies that $U_h^f = 0$. The source term approxi-

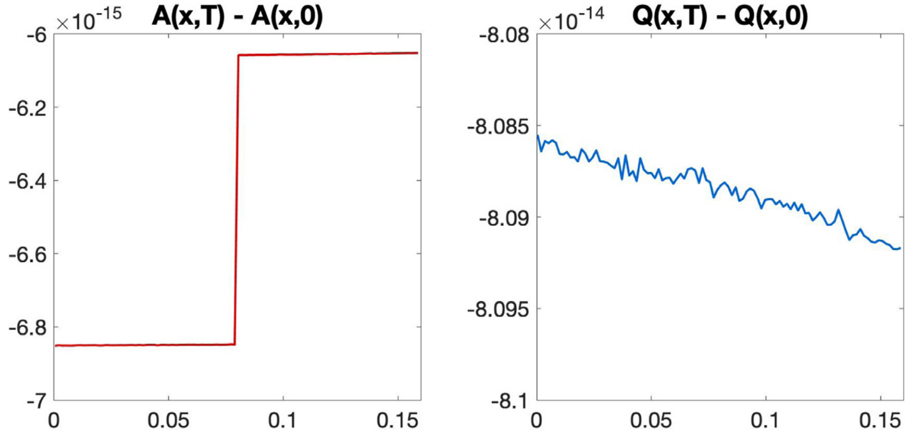

(a) Living-man well-balanced DG scheme

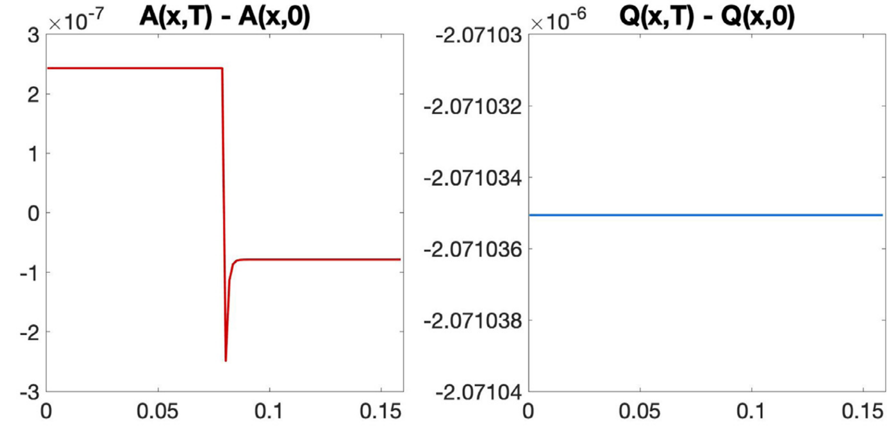

(b) Non-zero pressure man-at-eternal-rest well-balanced DG scheme

Fig. 18. The difference between A, Q at the final time $t = 5$ and the corresponding numerical initial conditions for the decreasing step problem with $S_{in} = 0.5$ from Section 5.2.3, when using the living-man well-balanced DG method (top row) and the man-at-eternal-rest well-balanced DG method (bottom row).

mation (4.17) can then be rewritten as

$$\int_{I_j} S(U_h, (A_0)_h)v\,dx = -\int_{I_j} f(U_h)v_x\,dx + f(U^-_{h,j+\frac{1}{2}})v^-_{j+\frac{1}{2}} - f(U^+_{h,j-\frac{1}{2}})v^+_{j-\frac{1}{2}} \tag{4.21}$$

The modified cell boundary values become

$$U^{*,-}_{h,j+\frac{1}{2}} = \begin{pmatrix} \max\left(0, A(\bar{V}_j, (A_0)^*_{j\pm\frac{1}{2}})\right) \\ \bar{m}^+_{j\pm\frac{1}{2}} \end{pmatrix} = U^{*,+}_{h,j+\frac{1}{2}}, \tag{4.22}$$

as a result of $U^f_h = 0$. Due to the consistency of the Lax–Friedrichs flux and the definition of the left and right fluxes, it can be shown that

$$\hat{f}^l_{j+\frac{1}{2}} = f(U^-_{h,j+\frac{1}{2}}), \quad \hat{f}^r_{j-\frac{1}{2}} = f(U^+_{h,j-\frac{1}{2}}) \tag{4.23}$$

at the steady state. Therefore, one can easily observe that the flux terms exactly balance the source term approximation, which shows the well-balanced property. □

This section concludes with two remarks about the well-balanced RKDG methods for the arterial blood flow model when the cross-sectional area at rest is constant, and the comparison of living-man and the man-at-eternal-rest well-balanced methods.

Remark 4.2. When the cross-sectional area at rest, A_0, is constant, the traditional DG scheme is recovered, that is, the source term approximation reduces to 0 and the left and right numerical fluxes reduce to the original fluxes. First, we look at the source term. Definition (4.9) implies that $U^e_{h,j} = \mathbb{P}_h U(\hat{V}_j, A_0) = constant$ in each cell I_j when $A_0 = constant$. Therefore, it can be shown that

$$\int_{I_j} S\left(U^e_h, (A_0)_h\right)v\,dx = -\int_{I_j} f\left(U^e_h\right)v_x\,dx + f\left(U^{e,-}_{h,j+\frac{1}{2}}\right)v^-_{j+\frac{1}{2}} - f\left(U^{e,+}_{h,j-\frac{1}{2}}\right)v^+_{j-\frac{1}{2}} = 0.$$

Additionally, $((A_0)_h)_x = 0$, hence, the numerical integral $\int_{I_j} S\left(U^f_h, (A_0)_h\right)v\ dx = 0$. Together, this implies the source term approximation is zero.

Second, we will show that the left and right numerical fluxes reduce to the original DG fluxes. When A_0 is constant, then $(A_0)^*_{h,j+\frac{1}{2}} = (A_0)^+_{h,j+\frac{1}{2}} = (A_0)^-_{h,j+\frac{1}{2}}$ which implies that $A\left(\hat{V}_j, (A_0)^*_{h,j+\frac{1}{2}}\right)$ recovers the original value of A^e_h at the cell interface exactly. Therefore,

$$\begin{aligned} A^{*,\pm}_{h,j+\frac{1}{2}} &= \max\left(0, A(\hat{V}_j, (A_0)^*_{h,j+\frac{1}{2}}) + A^{f,\pm}_{h,j+\frac{1}{2}}\right) \\ &= \max\left(0, A^{e,\pm}_{h,j+\frac{1}{2}} + A^{f,\pm}_{h,j+\frac{1}{2}}\right) = A^{\pm}_{h,j+\frac{1}{2}}. \end{aligned} \tag{4.24}$$

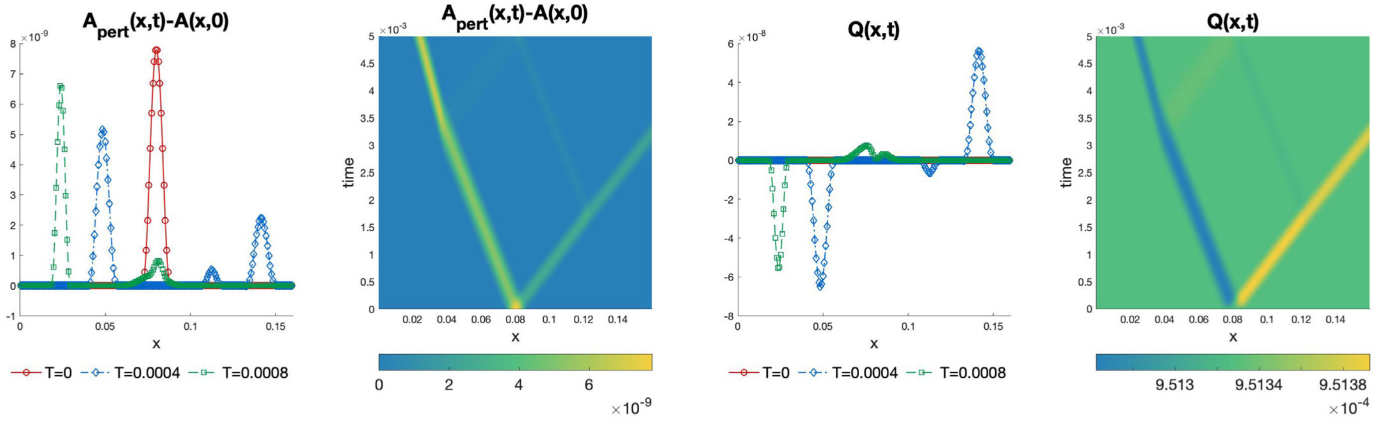

(a) $S_{in} = 0.5$

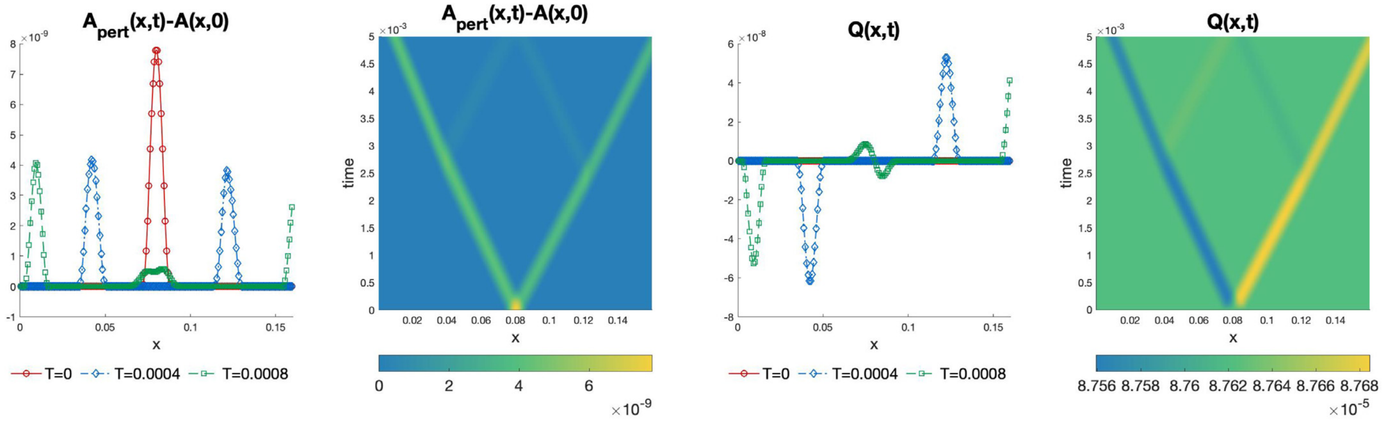

(b) $S_{in} = 0.1$

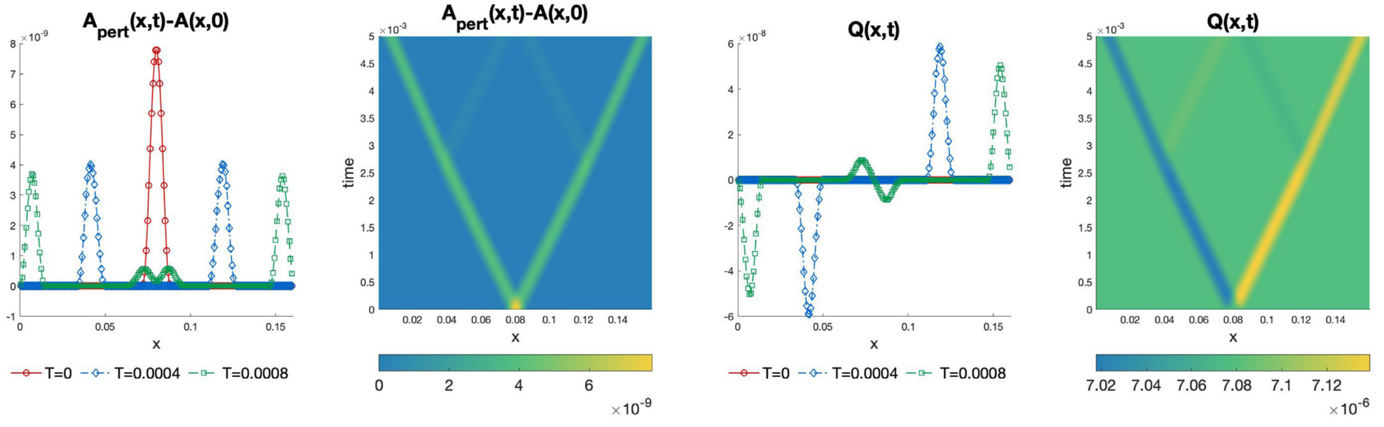

(c) $S_{in} = 0.01$

Fig. 19. The perturbation to the *aneurysm* problem for different values of S_{in} when the *living-man well-balanced scheme* is used. The two types of plots include snapshots of the solution at times $t = 0, 0.0025, 0.005,$ as well as plots that demonstrate how the perturbation propagates throughout the domain as a function of time. It can be seen that the larger the Shapiro number, the faster the perturbation propagates, especially the right moving wave. We can also see the formation of reflection waves.

More generally that $U^{*,\pm}_{h,j+\frac{1}{2}} = U^{\pm}_{h,j+\frac{1}{2}}$. Therefore the left and right numerical fluxes reduce to the original DG fluxes: $\hat{f}^{l}_{j+\frac{1}{2}} = \hat{f}_{j+\frac{1}{2}}$, $\hat{f}^{r}_{j-\frac{1}{2}} = \hat{f}_{j-\frac{1}{2}}$.

Remark 4.3. Although the well-balanced methods presented in this section were designed to preserve the living-man equilibria, it also preserve the simpler man-at-eternal-rest steady state. Notice that when $Q = 0$, the equilibrium values $\hat{V}_j$ become

$$\hat{V}_j = \begin{pmatrix} \hat{Q}_j \\ \hat{E}_j \end{pmatrix} = \begin{pmatrix} 0 \\ \beta\left(\sqrt{A_h} - \sqrt{(A_0)_h}\right)\left(x^{-}_{j+\frac{1}{2}}\right) \end{pmatrix}, \tag{4.25}$$

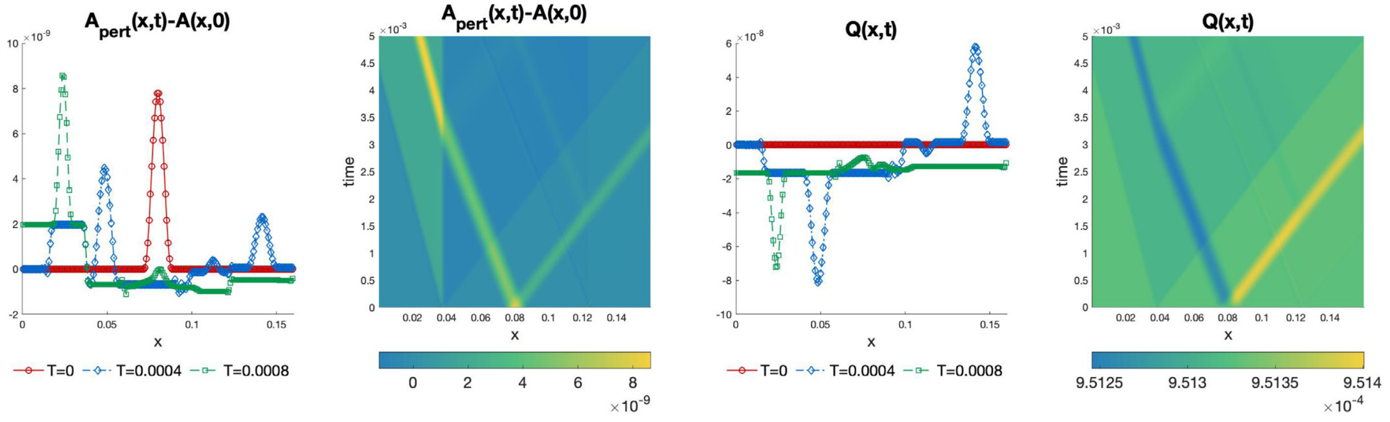

(a) $S_{in} = 0.5$

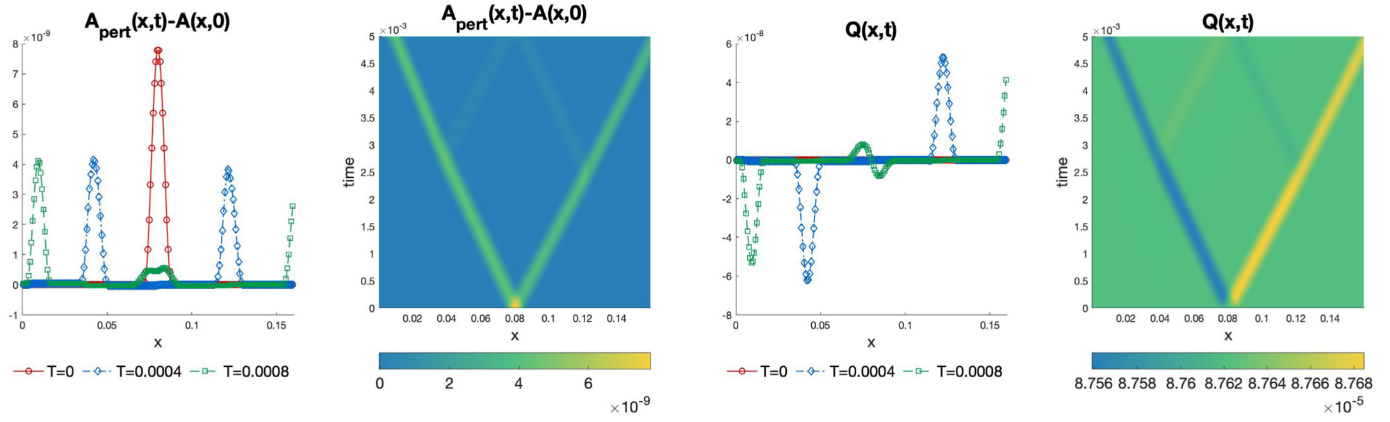

(b) $S_{in} = 0.1$

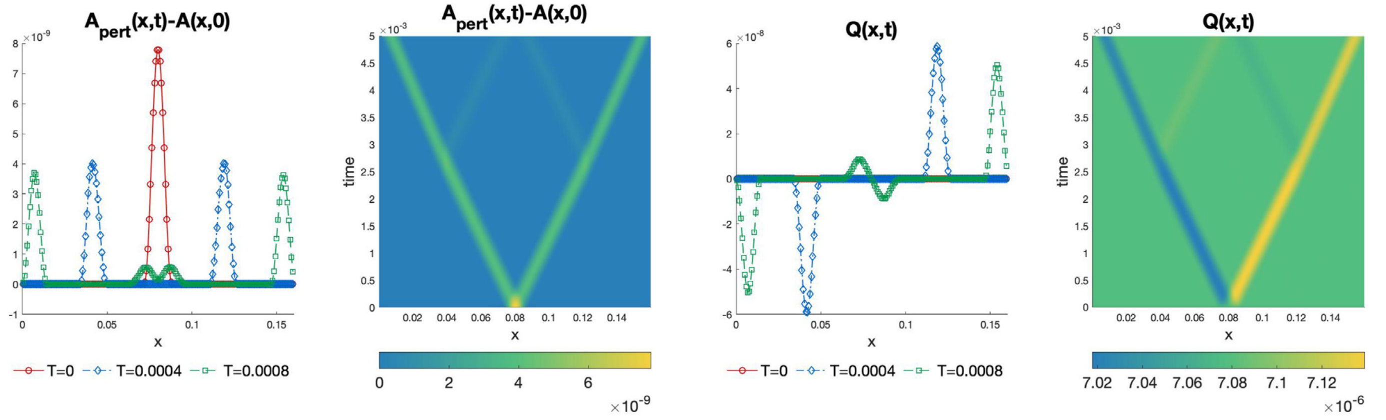

(c) $S_{in} = 0.01$

Fig. 20. The perturbation to the *aneurysm* problem for different values of S_{in} when the *man-at-eternal-rest well-balanced scheme* is used. The two types of plots include snapshots of the solution at times $t = 0, 0.0025, 0.005,$ as well as plots that demonstrate how the perturbation propagates throughout the domain as a function of time. It can be seen that the smaller the Shapiro number, the better the scheme performs because the living-man steady state becomes nearer to a non-zero pressure man-at-eternal-rest steady state.

and the decomposition of U, as in (4.9) and (4.10) becomes

$$U^e_{h,j} = \begin{pmatrix} \mathbb{P}_h\left(\frac{\hat{E}_j}{\beta} + \sqrt{(A_0)_h}\right)^2 \\ \hat{Q}_j \end{pmatrix},$$

$$U^f_{h,j} = \begin{pmatrix} A_{h,j} \\ Q_{h,j} \end{pmatrix} - \begin{pmatrix} \mathbb{P}_h\left(\frac{\hat{E}_j}{\beta} + \sqrt{(A_0)_h}\right)^2 \\ \hat{Q}_j \end{pmatrix}. \quad (4.26)$$

Therefore, the living-man well-balanced scheme reduces to the man-at-eternal-rest well-balanced scheme presented in Section 2.3.

5. Numerical tests for the living-man well-balanced methods

In this section, we present numerical results for the one-dimensional blood flow system (1.3) using the generalized living-

Table 8
L^1 errors and convergence orders of the accuracy test in Section 5.1, using P^0, P^1 and P^2 piecewise polynomials and the living-man well-balanced method. In each case, $k+1$ order of accuracy is achieved.

		$k=0$		$k=1$		$k=2$	
Variable	J	L^1 Error	Order	L^1 Error	Order	L^1 Error	Order
A	25	6.1773e-01		4.0942e-02		1.7301e-03	
	50	4.0751e-01	0.6002	1.0068e-02	2.0237	2.2514e-04	2.9420
	100	2.4607e-01	0.7278	2.5003e-03	2.0097	2.8747e-05	2.9693
	200	1.3667e-01	0.8484	6.2353e-04	2.0036	3.6285e-06	2.9860
	400	7.2197e-02	0.9207	1.5570e-04	2.0017	4.5571e-07	2.9932
Q	25	2.5275e02		6.2138e00		3.4179e-01	
	50	1.4838e02	0.7684	1.5290e00	2.0229	4.1730e-02	3.0340
	100	8.0758e01	0.8776	3.8080e-01	2.0055	5.1098e-03	3.0297
	200	4.2223e01	0.9356	9.5164e-02	2.0005	6.2939e-04	3.0212
	400	2.1591e01	0.9676	2.3794e-02	1.9998	7.8033e-05	3.0118

man well-balanced methods described in Section 4. We implement our scheme using piecewise quadratic polynomials ($k=2$) paired with the third order TVD Runge-Kutta time discretization (2.4). The CFL number is take to be 0.15 and the constant M in the TVB limiter is taken to be 0, unless otherwise stated. Multiple types of tests: accuracy test, well-balanced test, perturbations of steady states, and tests for discontinuous solutions, are presented in this section.

5.1. Accuracy test

In this section, we will test the accuracy of our living-man well-balanced DG scheme for smooth solutions with non-zero velocity. We have chosen strictly positive functions for both A and A_0 to avoid difficulties with square roots and division by a small number. The initial conditions in the domain $x \in [0, 10]$ are given by

$$A(x,0) = \sin\left(\frac{\pi}{5}x\right) + 10, \qquad Q(x,0) = e^{\cos(\frac{\pi}{5}x)}, \tag{5.1}$$

with the cross-sectional area at rest

$$A_0(x) = \frac{1}{2}\cos^2\left(\frac{\pi}{5}x\right) + 5,$$

and $K = 10^8\ \frac{Pa}{m}$, $\rho = 1060\ \frac{kg}{m^3}$. Periodic boundary conditions are employed in this test. We run the simulation until time $t = 0.01$ when the solution is still smooth. Since there is no explicitly known solution in this case, the errors are computed by comparing results from meshes of uniform cell widths h and $h/2$. Table 8 contains the L^1 errors and numerical orders of accuracy for P^0, P^1 and P^2 polynomials. For each polynomial degree k, $(k+1)^{\text{th}}$ order is observed, which indicates the optimal convergence rate is achieved.

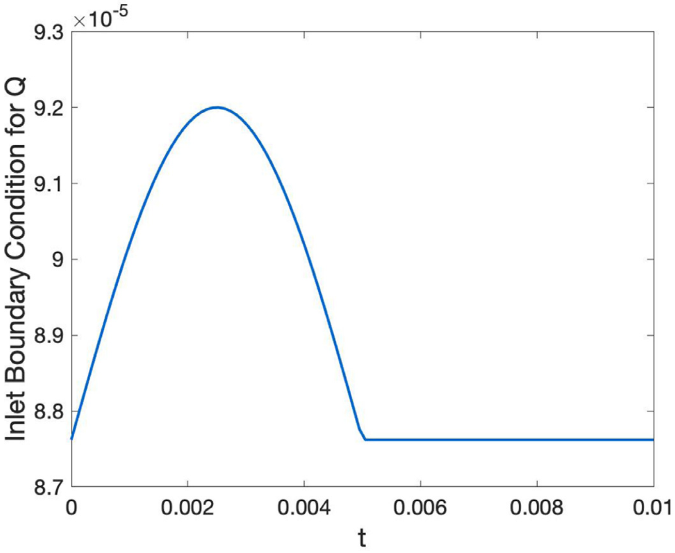

Fig. 21. The boundary condition (5.10) with $S_{in} = 0.1, \epsilon = 5 \times 10^{-2}$, and $T = 0.01$.

5.2. Test for well-balanced property

In this section, we will demonstrate that the proposed living-man well-balanced DG scheme preserves the steady state (1.7) with non-zero velocity. We will examine three examples that represent the physiological conditions of an aneurysm, stenosis, and a decreasing step. The initial conditions for each of the examples in this section will be determined from the equilibrium variables of the steady state, which take the form

$$Q_s = Q_{in}, \qquad E_s = \frac{Q_{in}^2}{2(A_{out})^2} + \beta\left(\sqrt{A_{out}} - \sqrt{(A_0(L)}\right), \tag{5.2}$$

where the subscript ‘in’ represents the value at the inlet or left side of the domain, ‘out’ represents the value at the outlet or the right side of the domain, and L is the length of the artery. The function for $A(x,\ 0)$ can be determined from (5.2) and the cross-sectional area at rest, which is unique to each example.

The values of A_{in} and A_{out} are given by

$$A_{in} = A_0(0)[1+S_{in}]^2, \qquad A_{out} = A_0(L)[1+S_{in}]^2, \tag{5.3}$$

where S_{in} is the Shapiro number at the inlet. The Shapiro number is the equivalent of the Froude number for the shallow water equations and is determined by the formula $S = u/C$ where C is the Moens–Korteweg wave velocity. The Shapiro number determines whether the system is in subcritical ($S < 1$), critical ($S = 1$), or supercritical ($S > 1$) flow. Blood flow is typically subcritical, hence that is the only case we will consider in the numerical examples. We will consider $S_{in} = \{0.5, 0.1, 0.01\}$ in our numerical examples. The Moens–Korteweg velocity at the inlet is defined as

$$C_{in} = \sqrt{\frac{K\sqrt{A_{in}}}{2\rho\sqrt{\pi}}}. \tag{5.4}$$

Finally, the value for Q_{in} can then be determined as a function of the Shapiro number in the following way

$$Q_{in} = A_{in}S_{h,in}C_{in}. \tag{5.5}$$

We also introduce the notation ΔR to represent the wall deformation parameter. Other important parameters in this section are found in Table 9. In each of the examples, we fix the boundary conditions to be Q_{in} at the inlet and A_{out} at the outlet of the domain.

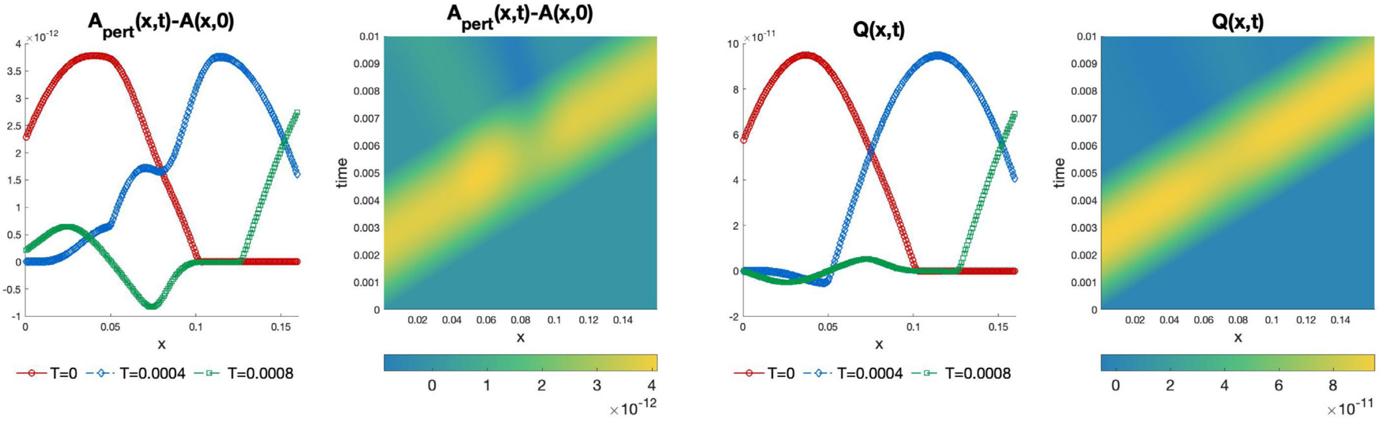

(a) $S_{in} = 0.5$

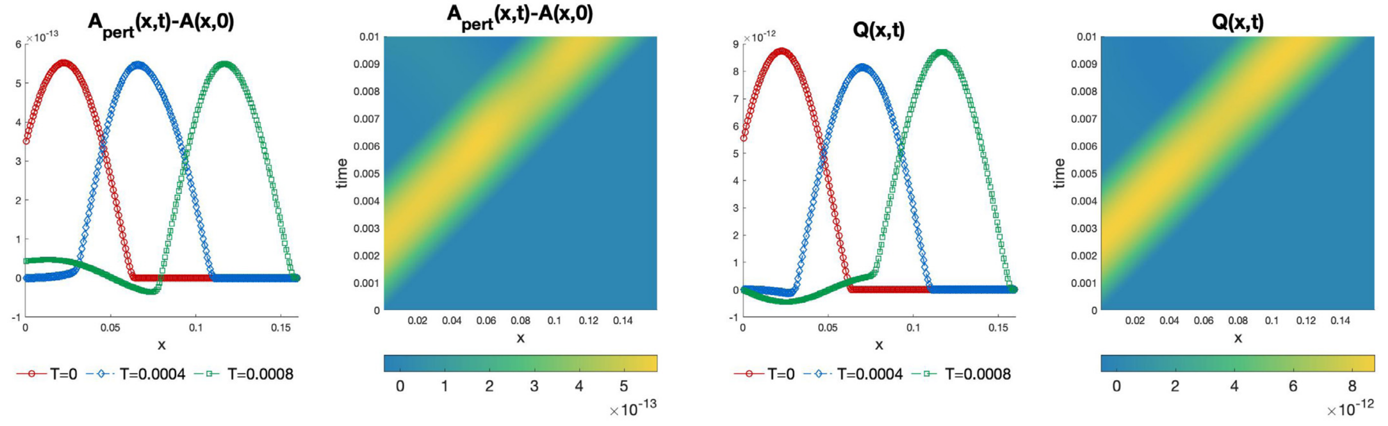

(b) $S_{in} = 0.1$

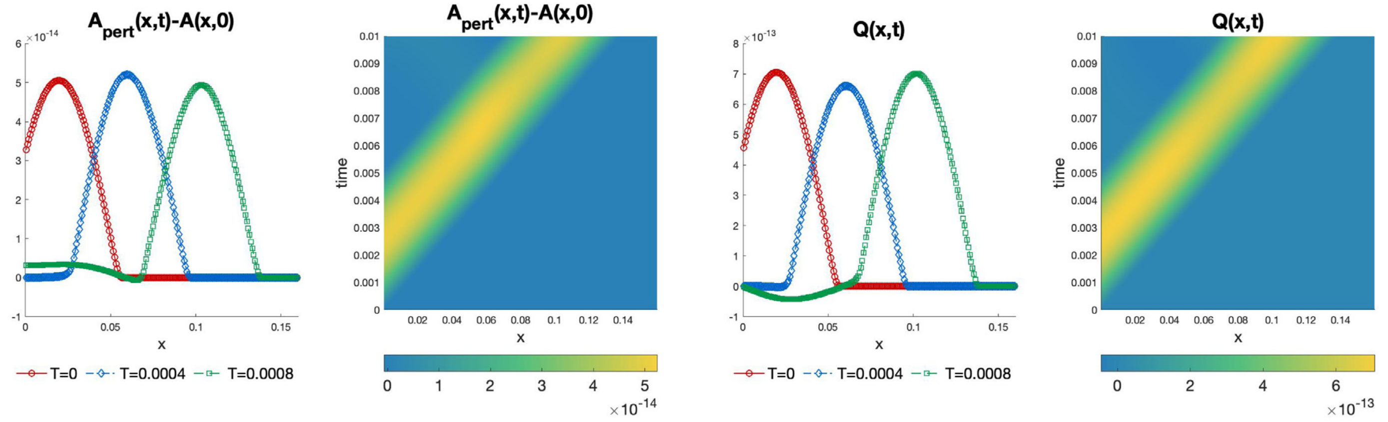

(c) $S_{in} = 0.01$

Fig. 22. The perturbation to the *stenosis* problem for different values of S_{in} when the *living-man well-balanced scheme* is used. The two types of plots include snapshots of the solution at times $t = 0.004, 0.007, 0.01,$ as well as plots that demonstrate how the perturbation propagates throughout the domain as a function of time. It can be seen that the larger the Shapiro number, the faster the perturbation propagates.

Table 9
Parameters for well-balanced living-man problems.

R_{in}	ΔR	K	ρ	L
$4 \times 10^{-3}\ m$	$1 \times 10^{-3}\ m$	$10^8\ \frac{Pa}{m}$	$1060\ \frac{kg}{m^3}$	$0.16\,m$

Table 10
The parameters used in the following examples that depend on the Shapiro number at the inlet, S_{in}. The smaller the Shapiro number S_{in}, the slower the discharge Q_{in}.

S_{in}	0.5	0.1	0.01
A_{in}	1.1310×10^{-4}	6.0821×10^{-5}	5.1276×10^{-5}
C_{in}	16.8232	14.4065	13.8046
Q_{in}	9.5133×10^{-4}	8.7622×10^{-5}	7.0784×10^{-6}

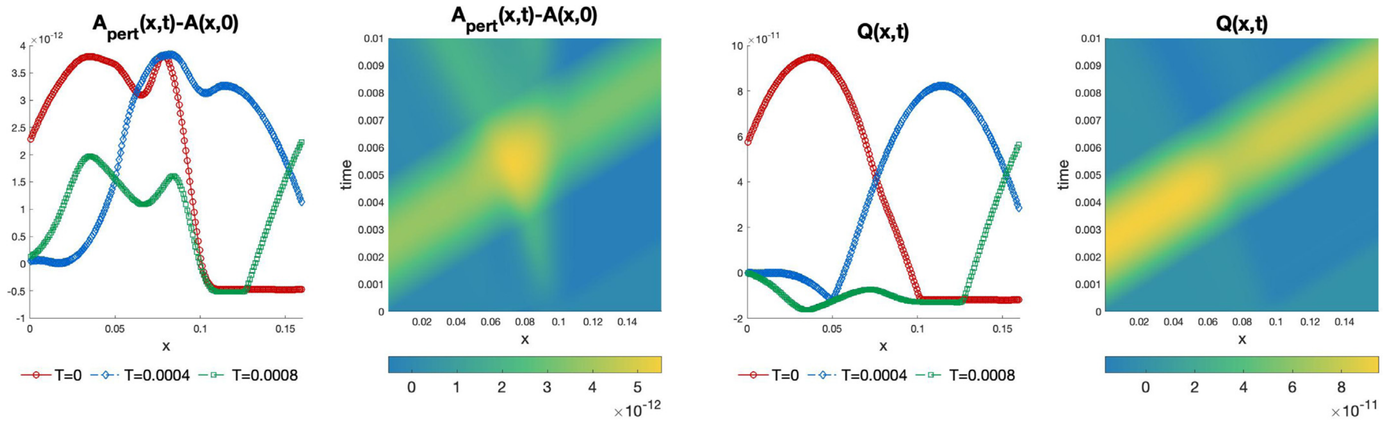

(a) $S_{in} = 0.5$

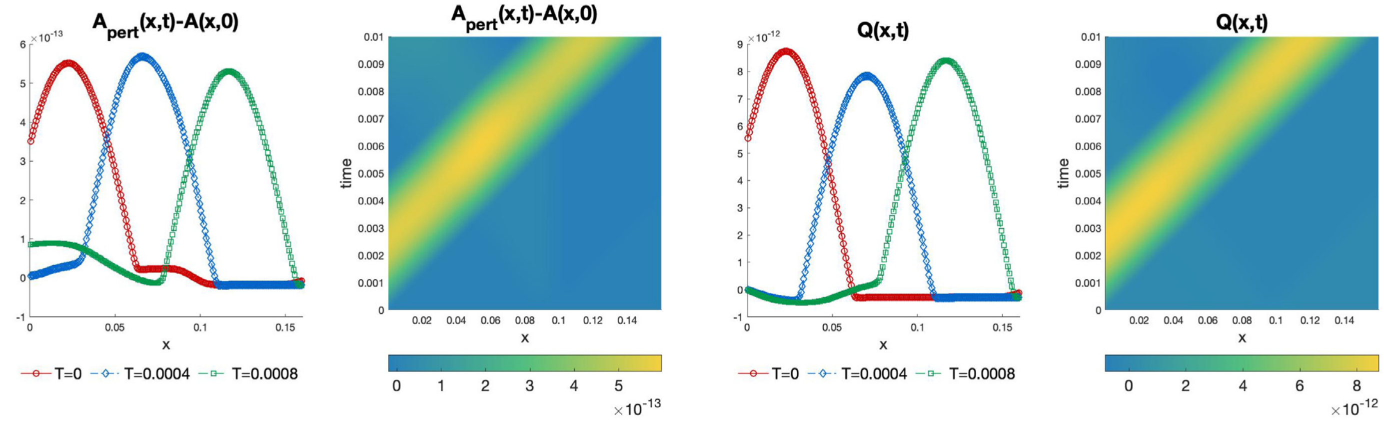

(b) $S_{in} = 0.1$

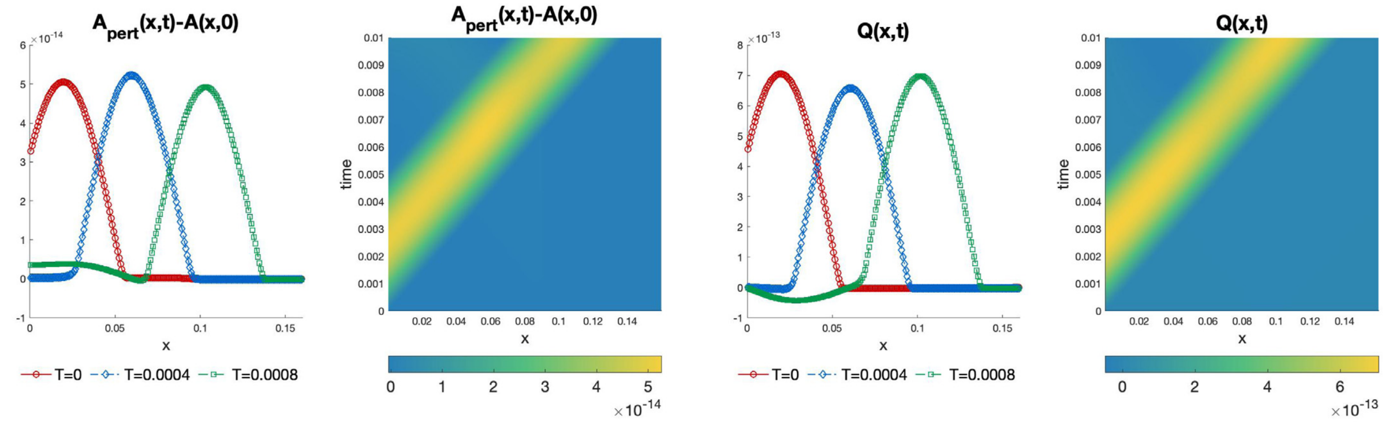

(c) $S_{in} = 0.01$

Fig. 23. The perturbation to the *stenosis* problem for different values of S_{in} when the *non-zero pressure man-at-eternal-rest well-balanced scheme* is used. The two types of plots include snapshots of the solution at times $t = 0.004, 0.007, 0.01,$ as well as plots that demonstrate how the perturbation propagates throughout the domain as a function of time.

Table 10 contains the some of the important constants used in the following examples. The constants all depend on the Shapiro number at the inlet. It can be seen that the smaller the Shapiro number, the slower the discharge value Q_{in}. We expect the living-man well-balanced scheme to maintain the steady states with machine zero error. The man-at-eternal-rest well-balanced scheme may not be able to preserve the non-zero velocity steady states. However, we expect the man-at-eternal-rest well-balanced scheme to perform better for lower Shapiro numbers because the lower the Shapiro number, the closer the living-man steady state will be towards the man-at-eternal-rest steady state (1.5) (i.e. zero velocity).

5.2.1. An aneurysm

In this subsection, we consider the living-man equilibrium (1.7) with non-zero velocity where the choice of cross-sectional radii is meant to represent that of an aneurysm. We set the cross-

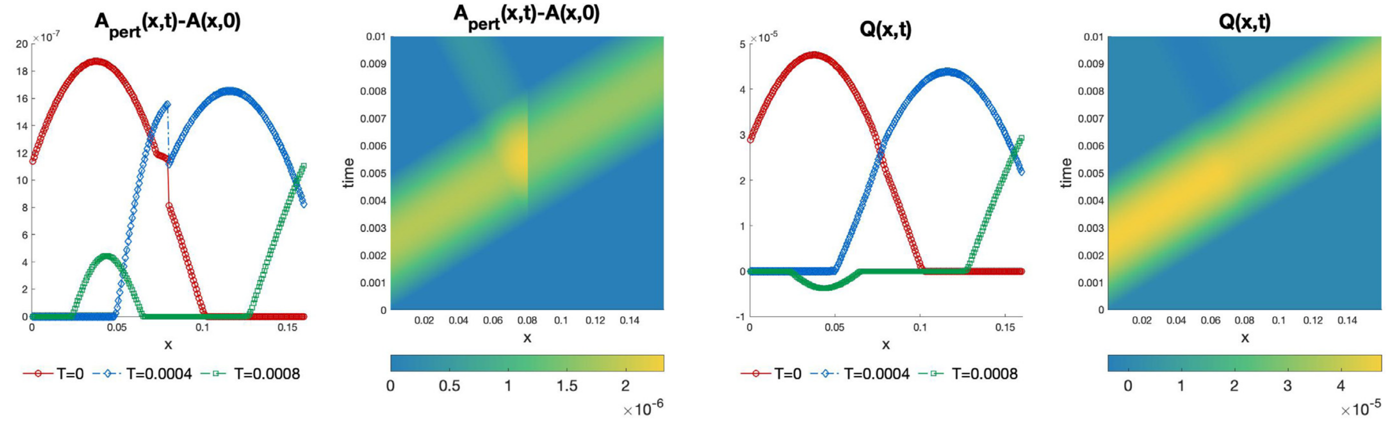

(a) $S_{in} = 0.5$

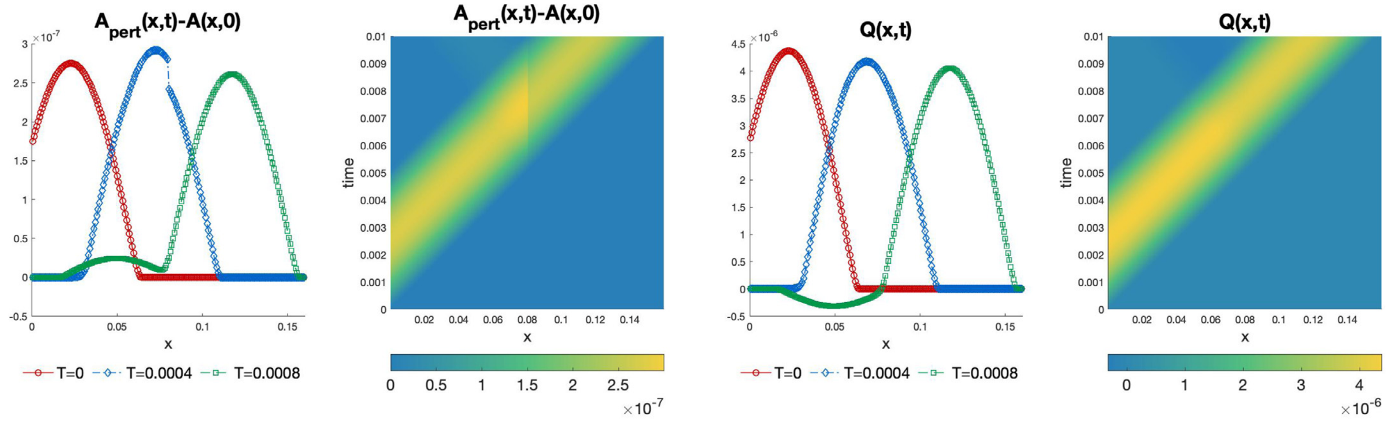

(b) $S_{in} = 0.1$

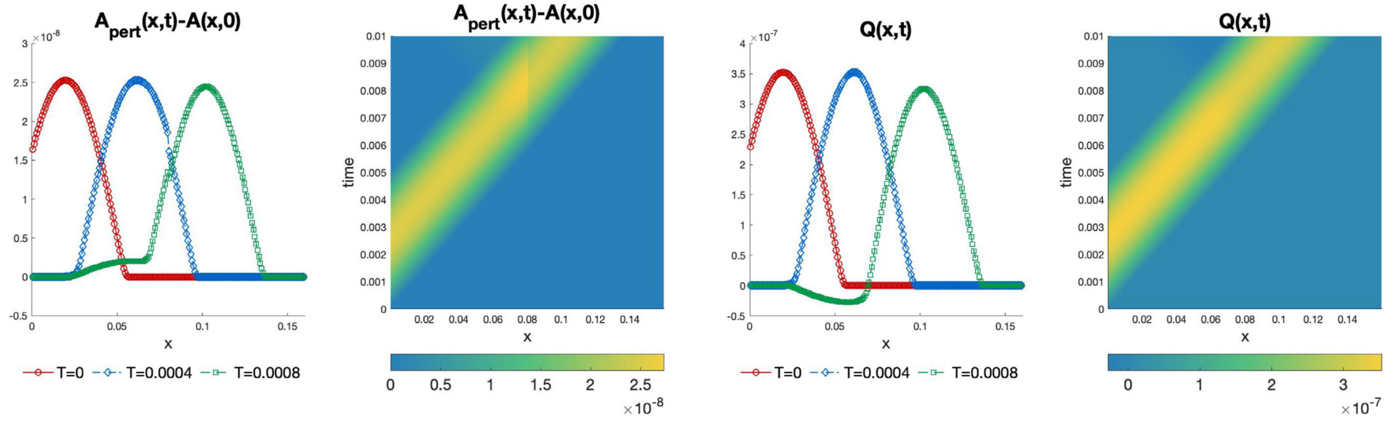

(c) $S_{in} = 0.01$

Fig. 24. The perturbation to the *decreasing step* problem for different values of S_{in} when the *living-man well-balanced scheme* is used. The two types of plots include snapshots of the solution at times $t = 0.004, 0.007, 0.01$, as well as plots that demonstrate how the perturbation propagates throughout the domain as a function of time.

sectional radii at rest to be

$$R_0(x) = \begin{cases} R_{in}, & \text{if } x \in [0, x_1] \cup [x_4, L], \\ R_{in} + \frac{\Delta R}{2}\left[1 - \cos\left(\frac{x - x_1}{x_2 - x_1}\pi\right)\right], & \text{if } x \in [x_1, x_2], \\ R_{in} + \Delta R, & \text{if } x \in [x_2, x_3], \\ R_{in} + \frac{\Delta R}{2}\left[1 + \cos\left(\frac{x - x_3}{x_4 - x_3}\pi\right)\right], & \text{if } x \in [x_3, x_4], \end{cases} \tag{5.6}$$

with $x_1 = \frac{9L}{40}, x_2 = \frac{L}{4}, x_3 = \frac{3L}{4}, x_4 = \frac{31L}{40}$ and the cross-sectional area at rest given by $A_0(x) = \pi R_0(x)^2$. The radii at rest is shown in Fig. 13.

The living-man equilibrium state should be exactly preserved. We run the problem using a uniform mesh of 200 cells until time $t = 5$. The L^1 and L^∞ errors shown in Table 11 demonstrate that the well-balanced property is indeed maintained. We also demonstrate that the man-at-eternal-rest well-balanced DG methods presented in Section 2 cannot maintain this general steady state with non-

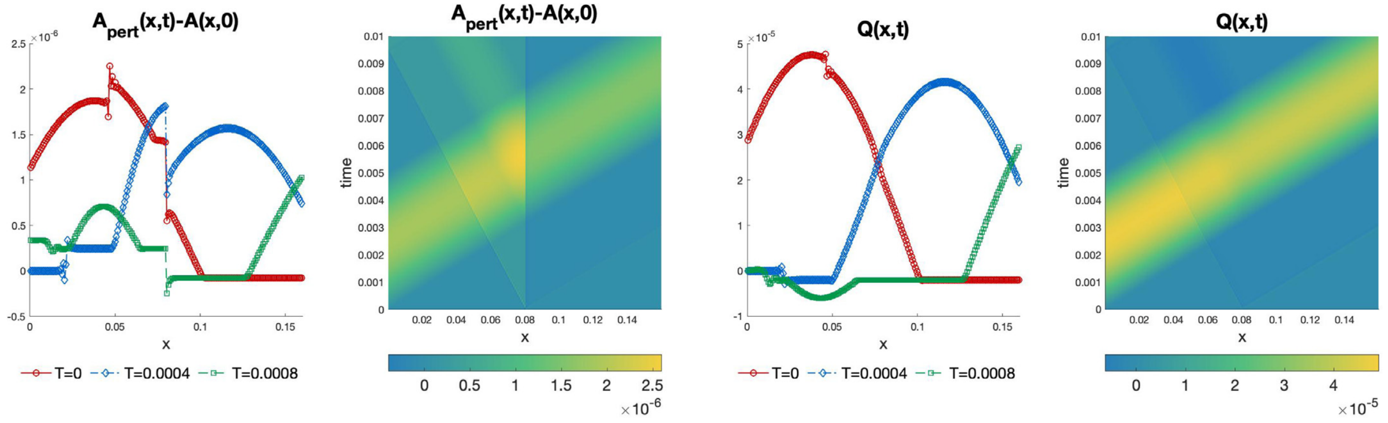

(a) $S_{in} = 0.5$

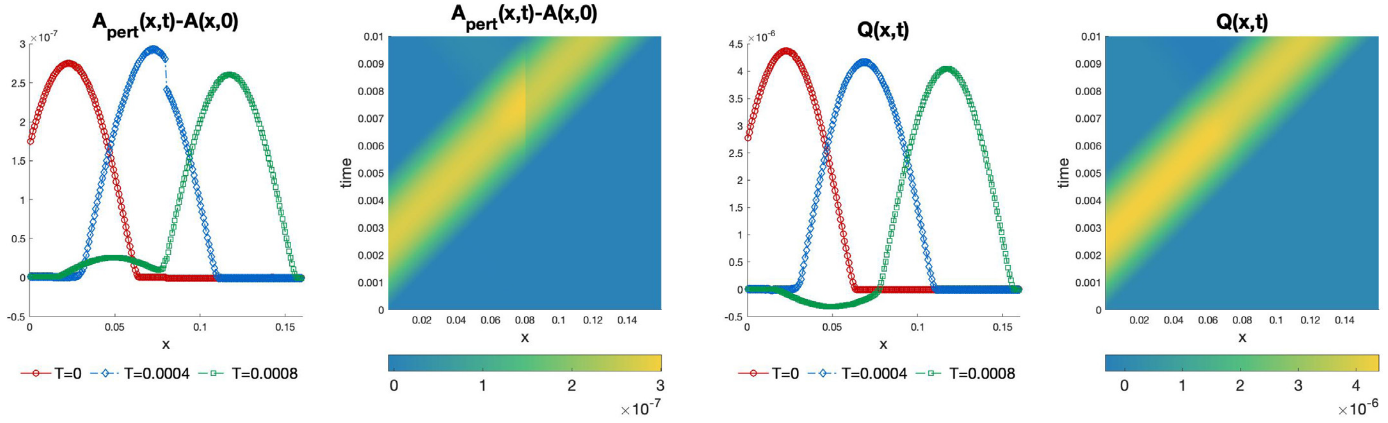

(b) $S_{in} = 0.1$

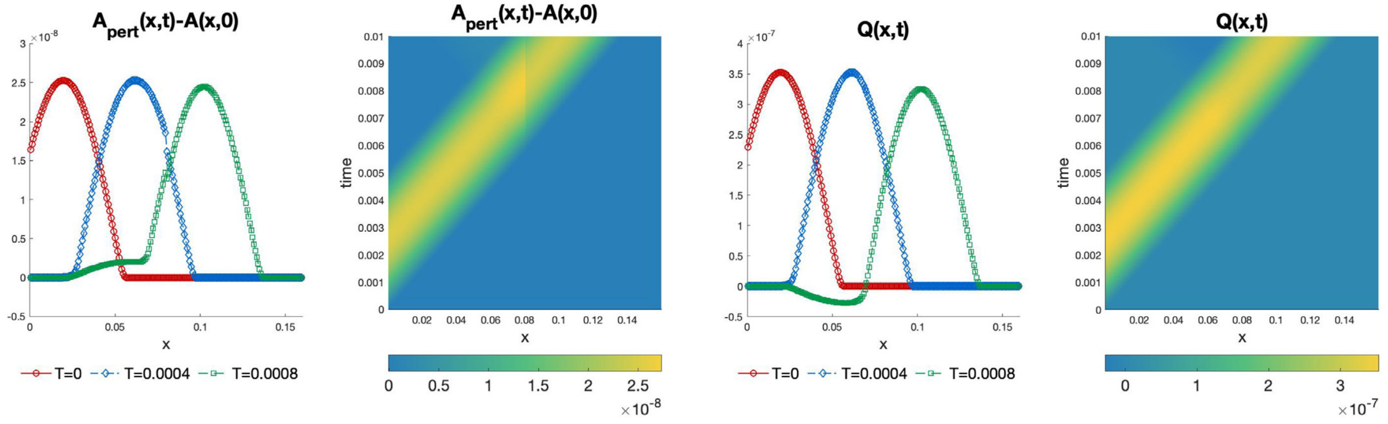

(c) $S_{in} = 0.01$

Fig. 25. The perturbation to the *decreasing step* problem for different values of S_{in} when the *non-zero pressure man-at-eternal-rest well-balanced scheme* is used. The two types of plots include snapshots of the solution at times $t = 0.004, 0.007, 0.01,$ as well as plots that demonstrate how the perturbation propagates throughout the domain as a function of time.

zero velocity for larger Shapiro numbers. The corresponding L^1 and L^∞ errors are found in Table 11 as well. The difference between the numerical solution at the final time $t = 5$ and the numerical initial conditions is plotted in Fig. 14, comparing both the living-man and man-at-eternal-rest well-balanced DG schemes when $S_{in} = 0.5$.

5.2.2. Stenosis

The function choice for the radius at rest representing aortic stenosis was first introduced in [14], and we changed to the parameters in this paper so that the units of measure are consistent with the units used in all other examples. The definition for the

Table 11
Table of absolute and relative L^1 and L^∞ errors for aneurysm problem in Section 5.2.1, using the living-man well-balanced scheme and the man-at-eternal-rest well-balanced scheme. The living-man scheme demonstrates the well-balanced property for each value of S_{in}. The man-at-eternal-rest DG scheme does not preserve the more general non-zero equilibrium state, but does improve as S_{in}, and thus Q_{in}, decreases.

		L^1 Error			L^∞ Error		
Variable	Error Type	$S_{in} = 0.5$	$S_{in} = 0.1$	$S_{in} = 0.01$	$S_{in} = 0.5$	$S_{in} = 0.1$	$S_{in} = 0.01$
Living-Man Well-Balanced Scheme							
A	Absolute	1.0083e-18	3.4893e-19	3.3321e-19	8.5896e-15	2.9880e-15	2.8745e-15
	Relative	7.3596e-15	4.6213e-15	5.1503e-15	6.2715e-11	4.0073e-11	4.4936e-11
Q	Absolute	9.3710e-18	3.4733e-19	1.4663e-19	7.3244e-14	2.7368e-15	1.1583e-15
	Relative	9.8505e-15	3.9640e-15	2.0715e-14	7.6992e-11	3.1234e-11	1.6363e-10
Man-at-Eternal-Rest Well-Balanced Scheme							
A	Absolute	1.5579e-13	4.1811e-15	4.0531e-17	1.8957e-08	2.4602e-10	1.9813e-12
	Relative	1.1679e-09	5.4732e-11	6.1572e-13	1.6030e-04	3.8299e-06	3.5730e-08
Q	Absolute	1.9450e-12	5.0298e-14	4.5631e-16	1.9807e-07	4.0129e-09	3.4643e-11
	Relative	2.0445e-09	5.7403e-10	6.4465e-11	2.0820e-04	4.5797e-05	4.8942e-06

Table 12
Table of absolute and relative L^1 and L^∞ errors for the stenosis problem in Section 5.2.2, using the living-man well-balanced scheme and the man-at-eternal-rest well-balanced scheme.

		L^1 Error			L^∞ Error		
Variable	Error Type	$S_{in} = 0.5$	$S_{in} = 0.1$	$S_{in} = 0.01$	$S_{in} = 0.5$	$S_{in} = 0.1$	$S_{in} = 0.01$
Living-Man Well-Balanced Scheme							
A	Absolute	9.3548e-19	2.9285e-19	2.5631e-19	7.4396e-15	2.3313e-15	2.0431e-15
	Relative	8.6103e-15	5.0023e-15	5.2088e-15	7.4199e-11	4.2203e-11	4.4224e-11
Q	Absolute	9.9849e-18	5.8225e-19	1.1724e-20	7.8033e-14	4.5572e-15	9.6175e-17
	Relative	1.0496e-14	6.6450e-15	1.6563e-15	8.2025e-11	5.2010e-11	1.3587e-11
Man-at-Eternal-Rest Well-Balanced Scheme							
A	Absolute	7.1488e-16	4.9425e-18	1.8366e-19	6.9856e-11	3.1689e-13	2.7633e-15
	Relative	7.2119e-12	8.6968e-14	3.7306e-15	7.3120e-07	6.0438e-09	6.2322e-11
Q	Absolute	6.2598e-15	8.6144e-17	8.4732e-19	4.5952e-10	4.6652e-12	3.9743e-14
	Relative	6.5801e-12	9.8313e-13	1.1971e-13	4.8303e-07	5.3242e-08	5.6147e-09

radius at rest is

$$R_0(x) = \begin{cases} R_{in}, & \text{if } x \in [0, x_1] \cup [x_2, L], \\ R_{in}\left(1 - \frac{\Delta R}{2}\left[1 + \cos\left(\pi + 2\pi \frac{x - x_1}{x_2 - x_1}\right)\right]\right), & \text{if } x \in [x_1, x_2], \end{cases} \tag{5.7}$$

where $x_1 = \frac{3L}{10}$ and $x_2 = \frac{7L}{10}$. The radii at rest is shown in Fig. 15.

The problem is computed until the final time $t = 5$ with a uniform mesh of 200 cells using both the living-man and man-at-eternal-rest well-balanced schemes. The L^1 and L^∞ errors shown in Table 12 and Fig. 16 displays the numerical solutions via the living-man and the man-at-eternal-rest schemes at the final time with $S_{in} = 0.5$.

5.2.3. Decreasing step

The example in this section represents blood flow from a parent to a daughter artery in which the transition is idealized, that is, the artery radii instantaneous changes from one value to a smaller value. The function choice for the radius at rest representing a decreasing step was first introduced in [14]. The radius at rest is given by

$$R_0(x) = \begin{cases} R_{in} & \text{if } x < \frac{L}{2}, \\ R_{in}(1 - \Delta R) & \text{if } x \geq \frac{L}{2}. \end{cases} \tag{5.8}$$

The radii at rest is shown in Fig. 17.

The problem is computed using both the living-man and man-at-eternal-rest well-balanced schemes with a uniform mesh of 200 cells until the final time $t = 5$. The L^1 and L^∞ errors shown in Table 13 demonstrate that the well-balanced property is indeed maintained for the living-man scheme, but not for the man-at-eternal-rest scheme. Fig. 18 displays the numerical solutions using both schemes with $S_{in} = 0.5$. Again, we observe that the man-at-eternal-rest well-balanced DG methods cannot maintain this general steady state with non-zero velocity well.

5.3. Nearly equilibrium flows

In this section, numerical tests are provided to demonstrate that the living-man well-balanced DG scheme can aptly handle small perturbations to living-man steady states, and capture the nearly equilibrium flows well. We will also compare the performance of the living-man and man-at-eternal-rest well-balanced schemes. Since each example from Section 5.2 contains arteries with non-constant area, we expect to see the formation of transmission and reflection pulses when the perturbation wave crosses through a portion of the domain that changes shape. The values of the reflection and transmission coefficients in (3.6) become valid only for small $S_{h,in}$ since they were derived from linear analytic solutions and the flow is now nonlinear.

5.3.1. Perturbation of A for the aneurysm

We consider a small perturbation to the living-man equilibrium state for an artery with an aneurysm, which was described in Section 5.2.1. The initial conditions can be determined from (5.2) and the cross-sectional radii at rest given by (5.6). The original initial condition for the cross-sectional area is denoted $A(x, 0)$

Table 13
Table of absolute and relative L^1 and L^∞ errors for the decreasing step test of in Section 5.2.3, using the living-man well-balanced scheme and the man-at-eternal-rest well-balanced scheme.

		L^1 Error			L^∞ Error		
Variable	Error Type	$S_{in} = 0.5$	$S_{in} = 0.1$	$S_{in} = 0.01$	$S_{in} = 0.5$	$S_{in} = 0.1$	$S_{in} = 0.01$
Living-Man Well-Balanced Scheme							
A	Absolute	8.2591e-19	2.697e-19	1.8666e-19	6.8517e-15	2.2094e-15	1.5366e-15
	Relative	8.0971e-15	4.9661e-15	4.0398e-15	6.5985e-11	4.0703e-11	3.3172e-11
Q	Absolute	1.0353e-17	4.8757e-19	1.1186e-18	8.0921e-14	3.8163e-15	8.7442e-15
	Relative	1.0883e-14	5.5644e-15	1.5802e-13	8.5061e-11	4.3554e-11	1.2353e-09
Man-at-Eternal-Rest Well-Balanced Scheme							
A	Absolute	2.4515e-11	1.0246e-13	2.9589e-16	4.0547e-06	5.8504e-08	4.7678e-10
	Relative	2.3512e-07	1.9215e-09	6.7841e-12	4.4164e-02	1.1875e-03	1.1455e-05
Q	Absolute	2.7844e-10	1.3728e-12	3.9381e-15	2.7728e-05	7.1167e-07	6.1411e-09
	Relative	2.9268e-07	1.5667e-08	5.5636e-10	2.9146e-02	8.1220e-03	8.6758e-04

and we denote the perturbed initial conditions of A by

$$A_{pert}(x,0) = A(x,0) + \pi\, p(x)^2,$$

where

$$p(x) = \begin{cases} \epsilon \sin\left(\frac{100}{10L}\pi\left(x - \frac{45L}{100}\right)\right), & \text{if } x \in \left[\frac{45L}{100}, \frac{55L}{100}\right], \\ 0, & \text{otherwise}, \end{cases} \tag{5.9}$$

with $\epsilon = 5 \times 10^{-5}$. The wave splits in two and moves in opposite directions away from the initial perturbation. The test is run with 200 uniform cells until the stopping time $t = 0.005$ and the solutions are shown in Fig. 19 for the living-man well-balanced scheme and in Fig. 20 for the man-at-eternal-rest well-balanced scheme. It can be seen that only in the case with $S_{in} = 0.5$, the man-at-eternal-rest well-balanced scheme does not handle the perturbation very well. This is because, for small Shapiro number, the living-man equilibrium state is near to a man-at-eternal-rest equilibrium, so the error in using the man-at-eternal-rest well-balanced scheme is smaller than the error that arises from the perturbation.

5.3.2. Inflow pulse to Q for an artery with stenosis & a discontinuous step

In this section we will simulate a pulse inflicted on the flow Q at the inlet of the domain. This pulse will be applied to both the stenosis and discontinuous step problems in Section 5.2. The initial conditions for both A and Q are determined in the same way as in Section 5.2, however we will introduce a different boundary condition for Q which simulates a pulse to the flow of blood. The boundary condition for Q at the inlet, denoted $\tilde{Q}_{in}$, is defined in the following way

$$\tilde{Q}_{in}(t) = \begin{cases} Q_{in}\left(1 + \epsilon \sin\left(2\pi \frac{t}{T}\right)\right) & \text{if } t \le \frac{T}{2}, \\ Q_{in} & \text{otherwise}, \end{cases} \tag{5.10}$$

where the pulse is inflicted until halfway through the computational time T, and then no more pulse is inflicted after that. This problem is similar to the one introduced in [14] with some modifications and the introduction of parameter ϵ. The value for Q_{in} is defined in (5.5) and depends on the Shapiro number $S_{in} = \{0.5, 0.1, 0.01\}$. We set the amplitude parameter $\epsilon = 1 \times 10^{-7}$ for the artery with stenosis and $\epsilon = 5 \times 10^{-2}$ for the decreasing step problem. The boundary condition is shown in Fig. 21.

All tests in this section are run until the final time of $t = 0.01$ with a mesh of 200 uniform cells. For each variation of the test, we will compare the performance of the living-man and man-at-eternal-rest well-balanced DG schemes. We present the results for an artery with stenosis in Figs. 22 and 23. Similarly to the aneurysm perturbation problem, the man-at-eternal-rest scheme handles the perturbation as well as the living-man scheme for $S_{in} = 0.1$ and 0.01. When $S_{in} = 0.5$, obvious error is observed in the numerical results of the man-at-eternal-rest well-balanced scheme. In Figs. 24 and 25, we list the numerical results for the decreasing step problem, using both living-man and man-

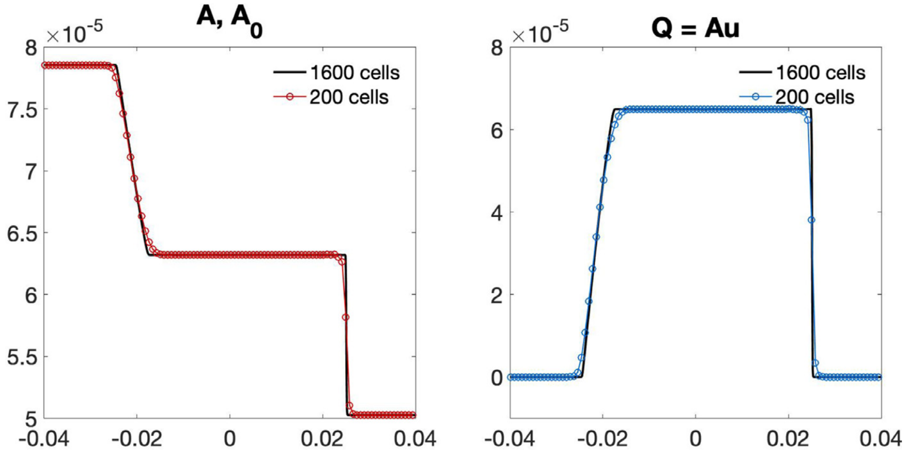

Fig. 26. Numerical solutions at time $t = 0.005$ with quadratic basis function and mesh sizes of 200 and 1600 uniform cells for the ideal tourniquet problem (5.11).

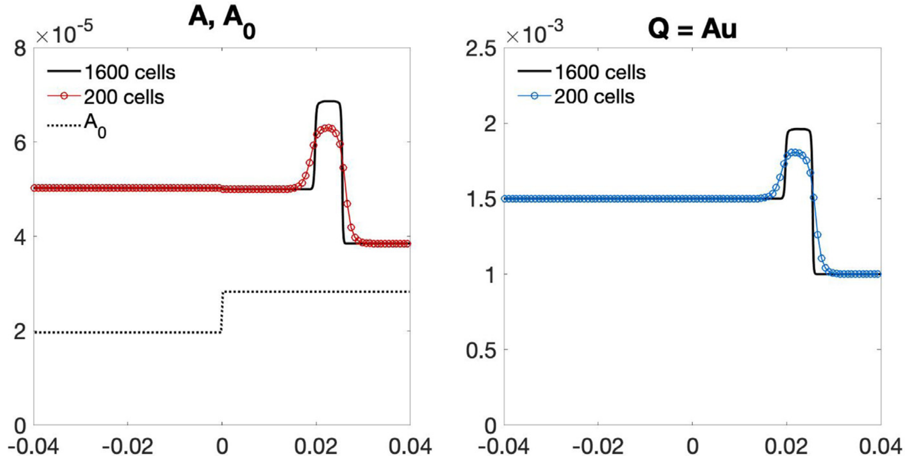

Fig. 27. Numerical solutions at time $t = 0.008$ with quadratic basis function and mesh sizes of 200 and 1600 uniform cells for the Riemann problem (5.12). TVB Minmod limiter is used.

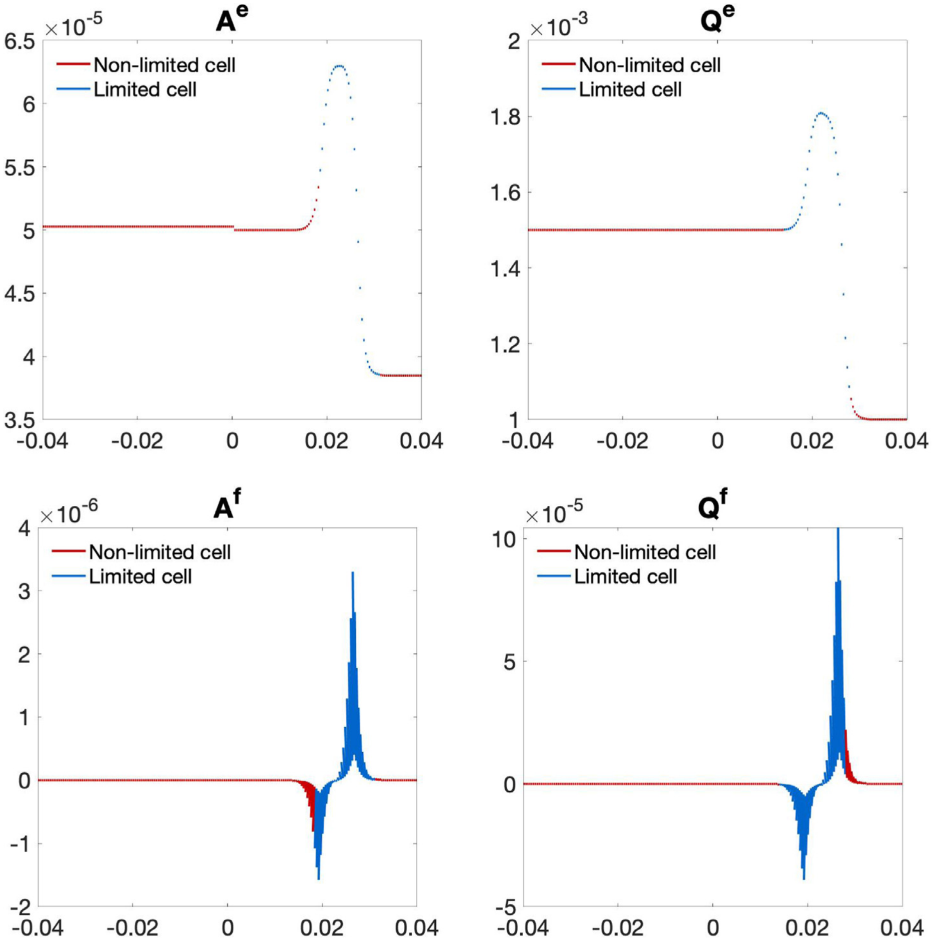

Fig. 28. Numerical solutions of U_h^e (top row) and U_h^f (bottom row) at time $t = 0.008$ with quadratic basis function and mesh size of 200 uniform cells for the Riemann problem (5.12). Cells in which the minmod limiter was applied after the last RK step are colored in blue and non-limited cells are colored red. (For interpretation of the references to colour in this figure legend, the reader is referred to the web version of this article.)

at-eternal-rest well-balanced DG schemes. Similar behavior can be observed.

5.4. Tests for discontinuous initial conditions

Two Riemann problems with discontinuous initial conditions will be considered in this section. We test the performance of the well-balanced DG methods in capturing discontinuous solutions.

5.4.1. The ideal tourniquet

Dam break problems are frequently studied for the shallow water equations. For the blood flow problem, the analogue is the ideal tourniquet problem. We consider a tourniquet that is applied and instantaneously removed. The computational domain for this problem is $[-0.04, 0.04]$ and the initial conditions are given by

$$A(x,0) = \begin{cases} \pi (R_{in})^2, & \text{if } x \le 0, \\ \pi (R_{out})^2, & \text{otherwise}, \end{cases} \qquad Q(x,0) = 0, \tag{5.11}$$

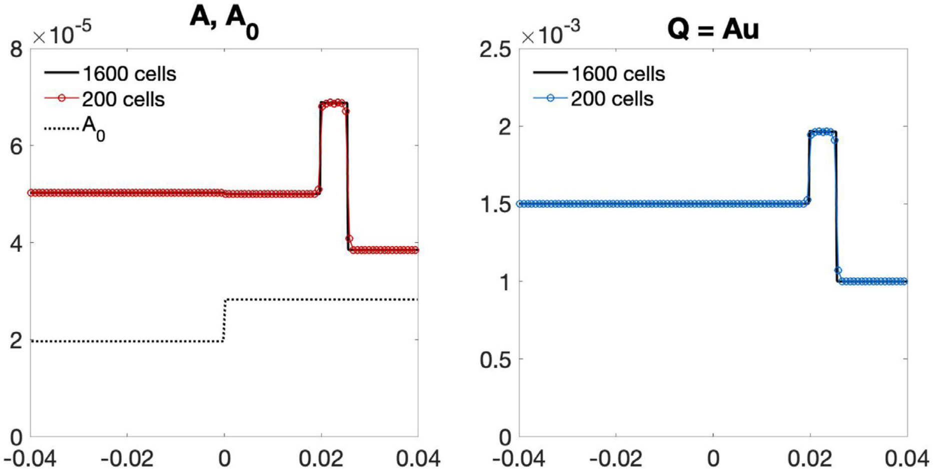

Fig. 29. Numerical solutions at time $t = 0.008$ with quadratic basis function and mesh sizes of 200 and 1600 uniform cells for the Riemann problem (5.12). The WENO limiter is used.

Table 14
Parameters for the ideal tourniquet problem (5.11) and the Riemann problem (5.12).

R_{in}	R_{out}	K	ρ
$5 \times 10^{-3}\ m$	$4 \times 10^{-3}\ m$	$10^7\ \frac{Pa}{m}$	$1060\ \frac{kg}{m^3}$

with the parameters listed in Table 14. The cross-sectional area at rest is defined as $A_0(x) = \pi(R_{out})^2$. Transmissive boundary conditions are implemented at the endpoints of the computational domain. The numerical solution is computed up to time $t = 0.005$. The discontinuity in the center becomes a shock wave propagating to the right and a rarefaction wave moving to the left. The numerical results with 200 uniform cells are presented in Fig. 26. For comparison, we also present the simulation results with refined 1600 uniform cells as a "reference" solution. We can see that the numerical solution agree well with the refined solutions. Our well-balanced DG methods can capture the shock wave well, and the slope limiter removes oscillatory near the discontinuities.

5.4.2. Riemann problem with non-flat radius at rest and non-zero velocity

Next, we consider a problem similar to the ideal tourniquet problem, but with a non-zero velocity and discontinuous cross-sectional area at rest given by

$$A(x,0) = \begin{cases} \pi(4 \times 10^{-3})^2, & \text{if } x \le 0, \\ \pi(3.5 \times 10^{-3})^2, & x > 0, \end{cases}$$

$$Q(x,0) = \begin{cases} 1.5 \times 10^{-3}, & \text{if } x \le 0, \\ 1 \times 10^{-3}, & \text{if } x > 0, \end{cases} \tag{5.12}$$

and

$$A_0(x) = \begin{cases} \pi(2.5 \times 10^{-3})^2, & \text{if } x \le 0, \\ \pi(3 \times 10^{-3})^2, & x > 0, \end{cases} \tag{5.13}$$

The computational domain for this problem is $[-0.04, 0.04]$ and the test is run until time $t = 0.008$. The numerical results with 200 uniform cells and TVB minmod limiter are presented in Fig. 27, and compared with the "reference" solution obtained with refined 1600 uniform cells. We can see that the numerical solution agrees well with the refined solutions. The minmod limiter marks the troubled cells based on U_h^f and performs the actual limiting procedure on U_h. We also plotted the figures of the decomposed solutions U_h^f and U_h^e at the final time in Fig. 28 in which the troubled cells marked by the limiter are distinguished from the non-limited cells. We have compared minmod slope procedure with the results of the standard minmod limiter (both trouble cell indicator and limiting on U_h), and observed the same results. In these figures, it can be seen that the shock profiles are smeared with 200 cells. For comparison, we also included the numerical results in Fig. 29 when WENO limiter is used instead, and this gives a sharp shock profile on the same mesh (200 cells).

6. Conclusion

In this paper we constructed and tested DG methods for the one-dimensional arterial blood flow system with the man-at-eternal-rest and living-man equilibria. Well-balanced DG methods are designed to efficiently capture the nearly equilibria flow which are small perturbation of these equilibrium states. We focus on the living-man equilibrium states which are more relevant to the practical problem. To construct well-balanced methods, special attention was paid to the projection of the initial conditions into piecewise polynomial space, the approximation of the source term, and the construction of the numerical fluxes. Extensive numerical examples were given to demonstrate the well-balanced property, accuracy, non-oscillatory behavior at discontinuities, and ability to resolve small perturbations to steady states. DG methods have been shown to be efficient for the hyperbolic balance laws on network, and it would be interesting to test the performance of the proposed methods on the arterial network blood flow simulations, which will be our future work.

Declaration of Competing Interest

The authors declare that they have no known competing financial interests or personal relationships that could have appeared to influence the work reported in this paper.

References

[1] Audusse E, Bouchut F, Bristeau M-O, Klein R, Perthame B. A fast and stable well-balanced scheme with hydrostatic reconstruction for shallow water flows. SIAM J Sci Comput 2004;25:2050–65.
[2] Bermudez A, Vazquez ME. Upwind methods for hyperbolic conservation laws with source terms. Comput Fluids 1994;23:1049–71.
[3] Boileau E, Nithiarasu P, Blanco P, Müller L, Fossan F, Hellevik L, et al. A benchmark study of numerical schemes for one-dimensional arterial blood flow modelling. Int J Numer Method Biomed Eng 2015;31(10):e02732.
[4] Buli J, Xing Y. A discontinuous Galerkin method for the Aw-Rascle traffic flow model on networks. J Comput Phys 2020;406:109183. doi:10.1016/j.jcp.2019.109183.

[5] Čanić S. Blood flow through compliant vessels after endovascular repair: wall deformations induced by the discontinuous wall properties. Comput Vis Sci 2002;4(3):147–55. doi:10.1007/s007910100066.

[6] Čanić S, Piccoli B, Qiu J-M, Ren T. Runge–Kutta discontinuous galerkin method for traffic flow model on networks. J Sci Comput 2015;63(1):233–55.

[7] Chandrashekar P, Klingenberg C. A second order well-balanced finite volume scheme for Euler equations with gravity. SIAM J Scientif Comput 2015;37:382–402.

[8] Delestre O, Lagrée P-Y. A well-balanced finite volume scheme for blood flow simulation. Int J Numer Methods Fluids 2013;72(2):177–205. doi:10.1002/fld.3736.

[9] Euler L. Principia pro motu sanguinis per arterias determinando. Opera Postuma 1862;2:814–23.

[10] Formaggia L, Gerbeau J-F, Nobile F, Quarteroni A. Numerical treatment of defective boundary conditions for the navier–Stokes equations. SIAM J Numer Anal 2002;40(1):376–401. doi:10.1137/S003614290038296X.

[11] Formaggia L, Gerbeau J, Nobile F, Quarteroni A. On the coupling of 3D and 1D navier-Stokes equations for flow problems in compliant vessels. Comput Methods Appl Mech Eng 2001;191(6):561–82. doi:10.1016/S0045-7825(01)00302-4.

[12] Formaggia L, Nobile F, Quarteroni A. A one dimensional model for blood flow: application to vascular prosthesis. In: Babuška I, Ciarlet PG, Miyoshi T, editors. Mathematical Modeling and Numerical Simulation in Continuum Mechanics. Berlin, Heidelberg: Springer Berlin Heidelberg; 2002. p. 137–53. ISBN 978-3-642-56288-4.

[13] Formaggia L, Quarteroni A, Veneziani A. Cardiovascular mathematics: modeling and simulation of the circulatory system. Springer-Verlag Italia, Milano; 2009.

[14] Ghigo A, Delestre O, Fullana J-M, Lagrée P-Y. Low-shapiro hydrostatic reconstruction technique for blood flow simulation in large arteries with varying geometrical and mechanical properties. J Comput Phys 2017;331:108–36. doi:10.1016/j.jcp.2016.11.032.

[15] Kurganov A. Finite-volume schemes for shallow-water equations. Acta Numerica 2018;27:289–351.

[16] Li G, Delestre O, Yuan L. Well-balanced discontinuous galerkin method and finite volume weno scheme based on hydrostatic reconstruction for blood flow model in arteries. Int J Numer Methods Fluids 2018;86(7):491–508. doi:10.1002/fld.4463.

[17] Li G, Xing Y. Well-balanced discontinuous galerkin methods with hydrostatic reconstruction for the euler equations with gravitation. J Comput Phys 2018;352:445–62.

[18] Lighthill MJ. Waves in fluids. Cambridge University Press Cambridge [Eng.]; New York; 1978. ISBN 0521216893 0521292336, http://www.loc.gov/catdir/toc/cam027/77008174.html.

[19] Murillo J, García-Navarro P. A roe type energy balanced solver for 1D arterial blood flow and transport. Comput Fluids 2015;117:149–67. doi:10.1016/j.compfluid.2015.05.003.

[20] Müller L, Parés C, Toro E. Well-balanced high-order numerical schemes for one-dimensional blood flow in vessels with varying mechanical properties. J Comput Phys 2013;242:53–85. http://www.sciencedirect.com/science/article/pii/S0021999113001277.

[21] Müller L, Toro EF. Well-balanced high-order solver for blood flow in networks of vessels with variable properties. Int J Numer Method Biomed Eng 2013;29(12):1388–411. doi:10.1002/cnm.2580.

[22] Noelle S, Xing Y, Shu C-W. High order well-balanced finite volume WENO schemes for shallow water equation with moving water. J Comput Phys 2007;226:29–58.

[23] Olufsen MS, Peskin CS, Kim WY, Pedersen EM, Nadim A, Larsen J. Numerical simulation and experimental validation of blood flow in arteries with structured-tree outflow conditions. Ann Biomed Eng 2000;28(11):1281–99. doi:10.1114/1.1326031.

[24] Pedley TJ. The fluid mechanics of large blood vessels. Cambridge University Press; 1980. doi:10.1017/CBO9780511896996.

[25] Pontrelli G. A mathematical model of flow in a liquid-filled visco-elastic tube. Med Biol Eng Comput 2002;40:550–6. doi:10.1007/BF02345454.

[26] Pontrelli G. Nonlinear pulse propagation in blood flow problems. In: Anile AM, Capasso V, Greco A, editors. Progress in Industrial Mathematics at ECMI 2000. Berlin, Heidelberg: Springer Berlin Heidelberg; 2002. p. 630–5. ISBN 978-3-662-04784-2.

[27] Quarteroni A, Tuveri M, Veneziani A. Computational vascular fluid dynamics: problems, models and methods. Comput Vis Sci 2000;2(4):163–97. doi:10.1007/s007910050039.

[28] Sherwin SJ, Formaggia L, Peiró J, Franke V. Computational modelling of 1d blood flow with variable mechanical properties and its application to the simulation of wave propagation in the human arterial system. Int J Numer Methods Fluids 2003;43(6–7):673–700. doi:10.1002/fld.543.

[29] Sherwin S, Franke V, Peiró J, Parker K. One-dimensional modelling of a vascular network in space-time variables. J Eng Math 2003;47(3):217–50.

[30] Shi Y, Lawford PV, Hose R. Review of Zero-D and 1-D models of blood flow in the cardiovascular system. Biomed Eng Online 2011;10(1):33.

[31] Wang Z, Li G, Delestre O. Well-balanced finite difference weighted essentially non-oscillatory schemes for the blood flow model. Int J Numer Methods Fluids 2016;82(9):607–22. doi:10.1002/fld.4232.

[32] Xiao N, Alastruey J, Alberto Figueroa C. A systematic comparison between 1-d and 3-d hemodynamics in compliant arterial models. Int J Numer Method Biomed Eng 2014;30(2):204–31.

[33] Xing Y. Exactly well-balanced discontinuous Galerkin methods for the shallow water equations with moving water equilibrium. J Comput Phys 2014;257:536–53.

[34] Xing Y, Shu C-W. High order finite difference WENO schemes with the exact conservation property for the shallow water equations. J Comput Phys 2005;208:206–27.

[35] Xing Y, Shu C-W. A new approach of high order well-balanced finite volume WENO schemes and discontinuous galerkin methods for a class of hyperbolic systems with source terms. Commun Comput Phys 2006;1:100–34.

[36] Xing Y, Shu C-W. High order well-balanced finite volume WENO schemes and discontinuous galerkin methods for a class of hyperbolic systems with source terms. J Comput Phys 2006;214:567–98.

[37] Xing Y, Shu C-W. High order well-balanced WENO scheme for the gas dynamics equations under gravitational fields. J Sci Comput 2013;54:645–62.

[38] Xing Y, Shu C-W. A survey of high order schemes for the shallow water equations. J Math Study 2014;47:221–49.

[39] Xing Y, Zhang X, Shu C-W. Positivity-preserving high order well-balanced discontinuous galerkin methods for the shallow water equations. Adv Water Resour 2010;33:1476–93.

[40] Young T. Hydraulic investigations, subservient to an intended croonian lecture on the motion of the blood. Philos Trans R Soc Lond 1808;98:164–86.